GENERATION OF VERSATILE VORTEX

LINEAR LIGHT BULLETS

Thesis

Submitted to

The School of Engineering of the

UNIVERSITY OF DAYTON

In Partial Fulfillment of the Requirements for

The Degree of

Master of Science in Electro-Optics

By

Xin Huang

UNIVERSITY OF DAYTON

Dayton, Ohio

December, 2015

GENERATION OF VERSATILE VORTEX LINEAR LIGHT BULLETS

Name: Huang, Xin

APPROVED BY:

Andy C. Chong, Ph.D. Advisory Committee Chairman Assistant Professor Physics Department and Electro-Optics Graduate Program	Imad Agha, Ph.D. Committee Member Assistant Professor Physics Department and Electro-Optics Graduate Program

Joseph W. Haus, Ph.D.
Committee Member
Professor
Electro-Optics Graduate Program

John G. Weber, Ph.D. Associate Dean School of Engineering	Eddy M. Rojas, Ph.D., M.A., P.E. Dean School of Engineering

ABSTRACT

GENERATION OF VERSATILE VORTEX LINEAR LIGHT BULLETS

Name: Huang, Xin
University of Dayton

Advisor: Dr. Andy C. Chong

We demonstrate a versatile vortex linear light bullet as a three-dimensional vortex Airy-Bessel wave packet for the first time. It combines a temporal Airy pulse with a higher order vortex Bessel beam in the spatial domain. Its non-varying feature in linear propagation is verified by three-dimensional (3D) measurements. Advanced from previously reported linear light bullets which are limited to specific materials, the vortex Airy-Bessel wave packet works as a light bullet for any material while carrying orbital angular momentum. It is believed that the versatile vortex linear light bullet is useful in many applications such as nano-lithography, nano-surgery, etc. The study of controlled collisions between optical vortices in the time domain is also reported in this thesis.

Dedicated to my parents and my girlfriend Veronique

ACKNOWLEDGEMENTS

I would like to express my special appreciation to my advisor Dr. Andy Chong, you have been a wonderful mentor for me. I would like to thank you for encouraging my research and for allowing me to grow as a researcher in past two years. Your advice on both research as well as on life have been invaluable. I would also like to sincerely thank my committee members, Prof. Haus and Dr. Agha for serving as my committee members. Thank you for the encouragements and suggestions. I also want to thank Prof. Zhan for assistance.

I would also like to thank my group members: Qian Cao, Chenchen Wan, Peiyun Li and other lovely friends in Electro-Optics Program, who have made valued contributions on my research. I really enjoy studying and working with you.

A special thanks to my family. I have a warm loving family. Their support has been powerful all the time, they encourage me every single moment and support me whenever I need it. I really appreciate their caring and loving me as I grow up.

TABLE OF CONTENTS

LIST OF FIGURES

LIST OF ABBREVIATIONS AND NOTATIONS

ABBREVIATIONS	DEFINITIONS
2D	Two-dimensional
3D	Three-dimensional
ps	Picosecond
fs	Femtosecond
nm	Nanometer
GVD	Group velocity dispersion
CW	Continuous wave
TL	Transform-limited
TOD	Third order dispersion
SVE	Slowly varying envelope
LG	Laguerre-Gaussian
SLM	Spatial light modulator
SHG	Second harmonic generation
AC	Auto-correlation
FWHM	Full-width half maximum
LC	Liquid-crystal
ITO	Indium tin oxide
CCD	Charge-coupled device
XC	Cross-correlation
NPE	Nonlinear polarization evolution

NOTATIONS	DEFINITIONS
E	Electric field in the time domain
A	Complex envelope
I	Optical intensity
w	Angular frequency
f	Frequency
φ	Temporal phase
Ẽ	Electric field in the frequency domain
S	Spectral intensity
ϕ	Spectral phase
k	Wavevector
λ	Wavelength
n	Refractive index
β	Propagation constant
v_g	Group velocity
β_2	Group velocity dispersion
β_3	Third order dispersion
τ	Temporal width
w	Beam width
L_D	Dispersion length
L_R	Diffraction length
Ai	Airy function
t_{gr}	Group velocity delay
J	Bessel function
l	Topological charge

CHAPTER I

INTRODUCTION

This thesis experimentally demonstrates a versatile vortex linear light bullet in the shape of a three-dimensional (3D) vortex Airy-Bessel wave packet. Its non-varying feature in linear propagation is verified by 3D measurements. In addition, the controlled collisions between optical vortices in the time domain are also studied using numerical simulations.

1.1 Organization of the thesis

There are five chapters in the thesis. Chapter I is the introduction of general linear light bullets. Starting with a background of 3D spatio-temporal wave packets. Studies of previously reported bullets in nonlinear and linear propagation are addressed. Some important linear light bullets are briefly discussed. Finally, the concept of versatile linear light bullets is introduced and discussed briefly. In addition, the concept of the optical vortex is also introduced.

Chapter II is the theoretical background of spatio-temporal wave packets and the versatile vortex linear light bullet. The chapter covers the theoretical description of spatio-temporal wave packets and their behaviors under the action of diffraction and dispersion effects. Two most important localized waves (Airy pulses and Bessel beams) are discussed in details in this chapter. In parallel, the description of optical vortices and their interactions in both the spatial and the temporal domains are discussed.

Chapter III discusses the experimental 3D wave packet diagnostics. At the beginning of the chapter, it describes typical methods to characterize ultrafast pulses and beam profiles separately. To characterize spatio-temporally coupled wave packets, 3D wave packet diagnostic is necessary. Advanced from typical diagnostics, a 3D wave packet profile measurement method used in experiments is discussed in details.

Chapter IV presents the experimental results of vortex Airy-Bessel wave packets as versatile linear light bullets. First, the experimental configuration to generate vortex Airy Bessel wave packets is presented. Numerical simulations and experimental measurement for the evolution of the vortex Airy-Bessel wave packets in linear propagation are presented. At the end of the chapter, a separate project of the collision of optical vortices in the time domain is introduced. Numerical simulations of the vortex collision in the time domain with future plans are discussed. Lastly, chapter V presents a short summary of the main findings during the project.

1.2 Optical spatio-temporal wave packets and linear light bullets

An optical spatio-temporal wave packet has a 3D intensity profile. Typically it can be well described as a combination of an ultrashort pulse in the temporal domain and a two-dimensional (2D) transverse wave-front profile in the spatial domain [1].

In general, ultrashort pulses refer to optical pulses with temporal widths in the femtosecond (fs) and the picosecond (ps) ranges. Ultrashort optical pulses are generated from mode-locked lasers. High power, ultrashort optical pulses have led to numerous scientific and technological developments. For instance, ultrafast pulses can be utilized in optical communication to improve the telecommunication speed. As another example, high power pulses that induce nonlinear signals from a sample can be utilized for

multiphoton microscopy [1]. For ultrashort optical pulses, pulse spreading in propagation is an inherent property of light that limits the applications of pulses. Ultrashort pulses broadening due to the dispersion effect can influence various applications such as the data fidelity in optical communication systems.

As the ultrafast pulse spreads, optical beams, which are transverse wave-front profiles, also spread as they propagate due to diffraction. The beam spreading due to diffraction is a well-known limiting factor for optical tweezers [2], high resolution image formation [3], free space communication [4], etc. Therefore, developing localized 3D wave packets which resist spatial and temporal broadening can be beneficial for many applications. Studying such localized spatio-temporal optical wave packets has been an interesting research topic for optics researchers. These 3D wave packets which resist the diffraction and dispersion effects are referred to as light bullets. Light bullets sustain their profiles in propagation by a balance among dispersion, diffraction and various nonlinear effects [5, 6].

In the nonlinear propagation, nonlinear light bullets exist when nonlinear effects simultaneously compensate dispersion and diffraction effects [7]. Nonlinear self-focusing effect is required to balance the spatial spreading while the nonlinear self-phase modulation, which is an intensity-dependent refractive index, is to balance the temporal broadening effect. One-dimensional nonlinear light bullets such as optical solitons (temporal solitons) in fibers are experimentally realized by maintaining a balance between the self-phase modulation and the anomalous group velocity dispersion (GVD) [8, 9]. Moreover, 2D spatial solitons have been experimentally demonstrated by Segev *et al* in photorefractive media [10]. However, 3D spatio-temporal optical solitons tend to be

unstable since they require precise balance between nonlinear and 3D linear effects. Hence, generation of 3D nonlinear light bullets is a great challenge [6, 11].

In linear propagation, 3D spatio-temporal linear light bullets have been demonstrated in a variety forms such as X-waves and O-waves in medium with normal dispersion and anomalous dispersion respectively. The propagation invariant behavior relies on a balance between the dispersion and diffraction effect. Liner light bullets, such as X-wave and O-waves, are exact propagation invariant solutions to the Helmholtz equation. However, the perfect solutions cannot be realized experimentally since they require infinite amount of energy. Even though the perfect solutions are not possible, truncated solutions with limited energies still propagate as linear light bullets over a finite distance. Applications of these propagation invariant waves include acoustic imaging, electromagnetic energy transmission, etc. [12, 13].

Since such linear light bullets rely on the balance between dispersion and diffraction effects, they only work for specific materials. Besides, the spatial and the temporal profile of the wave packet are highly coupled in general: the temporal profile depends on the spatial location. The spatio-temporal coupling have led to a variety of linear light bullets such as Bessel-X pulses [14] and pulsed Bessel beams [15] as a superposition of polychromatic Bessel beams with a cone angle dispersion. These tailored waves can propagate with strong spatial and temporal localization in proper dispersive media. However, such wave packets require a specific group velocity dispersion (GVD) to cancel the cone-angle dispersion of Bessel beams. Therefore, a wave packet such as a Bessel X-wave works as a linear light bullet only for a certain medium.

A novel linear light bullet that is not limited to a specific medium is worthy of further investigations. The only way to realize such light bullet is to compensate the diffraction and dispersion effects separately. This can be achieved by forming non-dispersive wave packets in temporal dimension. The only one dimensional (1D) propagation invariant solution of the paraxial equation turns out to be an Airy function. The first propagation invariant Airy function in the spatial domain as an Airy beam was demonstrated by Siviloglou *et al*. [16]. In contrast to traditional non-diffractive beams, such as Bessel beams, Airy beams do not rely on the ensemble of plane waves with wavevectors lying on the surface of a cone. Moreover, Airy waves have unique properties such as self-acceleration [16] and self-healing [17]. Chong *et al.* demonstrated a linear light bullet combining a Bessel beam with an Airy temporal pulse [18]. This Airy-Bessel wave packet does not require the balance between the dispersion and diffraction effects since Airy pulses and Bessel beams are impervious to the dispersion and diffraction respectively. Since Airy-Bessel wave packets work as light bullets for any linear medium, they are referred to as 'versatile' linear light bullets.

An optical vortex is a special beam possessing a spatial phase as a function of the azimuthal angle. Such beams carry orbital angular momentums which can be useful in particle manipulation, free space telecommunication, micromachining, quantum information security and quantum entanglement of photons [19-21]. Optical vortices are also useful in nonlinear optics. For example, stable optical vortex solitons have been demonstrated in a nonlinear medium [22, 23].

In this thesis, we demonstrate a versatile vortex linear light bullet as a vortex Airy-Bessel wave packet advanced from the Airy-Bessel wave packet. The vortex Airy-

Bessel wave packet contains an Airy pulse in the temporal domain and a higher order Bessel beam profile in the spatial domain. It also contains the azimuthal phase dependency and therefore it has a phase singularity at the beam center. In particular, its 3D non-varying feature in linear propagation is verified by the 3D intensity profile and the transverse phase profile measurement. Since the temporal and the spatial profiles are separable, the vortex Airy-Bessel wave packets are suitable for a wide range of materials with various dispersion and diffraction parameters.

Studying interactions between optical beams carrying angular momentum is an interesting topic. The interaction of vortices may lead to repulsion, creation and annihilation of phase singularities. So far the controlled collisions between vortices in the spatial domain have been reported by Rosales-Guzman *et al* [24]. Another work in this thesis is to study the controlled collisions between optical vortices in the temporal domain. In order to study the interaction effects between vortices (repulsion, attraction, annihilation, etc.), simulations are performed on the controlled collisions between the wave packets carrying optical vortices.

CHAPTER II

THEORETICAL BACKGROUND

The purpose of this chapter is to present the theoretical background of the versatile vortex linear light bullet. Theoretical treatment of highly localized Airy and Bessel waves are presented. Optical vortices and their interactions are also addressed.

2.1 Spatio-temporal wave packets

Optical spatio-temporal wave packets have 3D intensity profiles. In the time domain, the pulse profile of the wave packet can be expressed by

$$E(t) = A(t)\exp(jw_0 t), \quad (2\text{-}1)$$

where $A(t)$ is the complex envelope function, which is characterized by a magnitude $|A(t)|$ and a temporal phase term $\varphi(t)$. $w_0 = 2\pi f_0$ is the central angular frequency of the wave packet where f_0 is the central frequency. The pulse profile is given by

$$E(t) = |A(t)|\exp\big(jw_0 t + j\varphi(t)\big). \quad (2\text{-}2)$$

The optical intensity is given by

$$I(t) = |A(t)|^2. \quad (2\text{-}3)$$

An optical pulse is well approximated by a Gaussian function.

$$I(t) \propto e^{-\frac{t^2}{\tau_0^2}}. \quad (2\text{-}4)$$

τ_o, which is the temporal half-width at 1/e of the intensity maximum, indicates the pulse duration. Besides a Gaussian function, a Lorentzian function and a parabolic function are also used as pulse profile functions [1].

In the frequency domain, its spectral profile can be obtained by Fourier transform of $E(t)$

$$\tilde{\mathrm{E}}(w)=\int_{-\infty}^{\infty} E(t)\exp(-jwt)\,dt, \qquad (2\text{-}5)$$

The resulting spectral profile can be expressed as

$$\tilde{\mathrm{E}}(w) = |\tilde{\mathrm{E}}(w)|\exp\big(j\phi(w)\big), \qquad (2\text{-}6)$$

where $|\tilde{\mathrm{E}}(w)|$ is the spectral magnitude and $\phi(w)$ is the spectral phase.

Similarly, the spectral intensity is given by

$$S(w) = |\tilde{\mathrm{E}}(w)|^2. \qquad (2\text{-}7)$$

In ultrafast optics, spatio-temporal wave packets have ultra-short pulses (picosecond (ps) or femtosecond (fs) level) with abroad spectra [1].

On the other hand, in the spatial domain, the beam profile of a monochromatic wave can be expressed by

$$E(x,y) = A(x,y)\exp\big(-j(k_x x + k_y y)\big), \qquad (2\text{-}8)$$

where $A(x,y)$ is a complex beam envelope characterized by a magnitude $|A(x,y)|$ and a spatial phase term $\varphi(x,y)$. x and y represent the spatial coordinates. The wavevector (or spatial angular frequencies) are given by $k_x = 2\pi v_x$ and $k_y = 2\pi v_y$ where v_x and v_y (cycles per unit length) are the spatial frequencies. In the spatial frequency domain, the spatial spectral distribution of a monochromatic wave can also be obtained by Fourier transform of the spatial envelope function $E(x,y)$.

$$\tilde{\mathrm{E}}\big(k_x,k_y\big)=\iint_{-\infty}^{\infty} E(x,y)\exp\Big(-j\big(k_x x + k_y y\big)\Big)\,dxdy, \qquad (2\text{-}9)$$

2.2 Group velocity dispersion and diffraction

When a pulse propagates in a dispersive medium, the index of refraction of the medium is a function of the pulse wavelength. This phenomenon is referred to as dispersion [25]. Group velocity dispersion (GVD) plays an important role in ultrafast pulses because ultrashort pulses are broadened significantly by GVD. Other types of dispersions such as modal dispersion and polarization mode dispersion [26], which are particularly related to optical waveguides, are not covered in this thesis.

In a dispersive medium, the effect of dispersion can be expressed by expanding the propagation constant $\beta(w)$ around the central frequency w_0 in a Taylor series [27].

$$\beta(w) = n(w) \cdot \frac{w}{c} = \beta_0 + \beta_1(w - w_0) + \frac{1}{2}\beta_2(w - w_0)^2 + \frac{1}{6}\beta_3(w - w_0)^3 \ldots \quad (2\text{-}10)$$

The parameter β_1 in equation (2-10) is related to the group velocity ($v_g = \beta_1^{-1}$) which accounts for the velocity of the pulse envelope in the medium. The group velocity provides an effective way to look at the traveling speed of the pulse envelope.

The parameter β_2 in equation (2-10), which is the derivative of β_1(or v_g) with respect to the angular frequency, is referred to as the group velocity dispersion (GVD) coefficient. GVD is the main term that characterizes the pulse broadening. As the GVD influences a pulse, the carrier frequency under the pulse envelope changes linearly across the pulse. The change of the carrier frequency as a function of time is referred to as the frequency chirp. In general, shorter pulses broaden more rapidly in propagation since such pulses have wider spectra.

The GVD effect can be expressed as a parameter called a dispersion length. Here we consider a Gaussian pulse whose electric field is given by

$$E(t) = e^{-\frac{t^2}{2\tau_0^2}}, \quad (2\text{-}11)$$

where τ_0 is the half width at *1/e* intensity pulse duration. The dispersion length is expressed by

$$L_D = \left|\frac{\tau_0^2}{\beta_2}\right|. \qquad (2\text{-}12)$$

The shorter dispersion length corresponds to the larger GVD effect on the pulse. By comparing the dispersion length to the propagation distance, one can estimate the broadening effect on the initial transform-limited (unchirped) Gaussian pulse. The pulse duration τ of a Gaussian pulse after propagation distance z is given by [1]

$$\tau(z) = \tau_0\sqrt{1 + (\frac{z}{L_D})^2}. \quad (2\text{-}13)$$

Figure 2.1 illustrates the pulse broadening effect in a dispersive medium. From the figure, one can see that the initial pulse width τ_0 increases along as it propagates. After the pulse propagates in a medium for one dispersion length ($z = L_D$), the pulse is broadened by a factor of $\sqrt{2}$. The pulse width will be doubled at $z = \sqrt{3}L_D$.

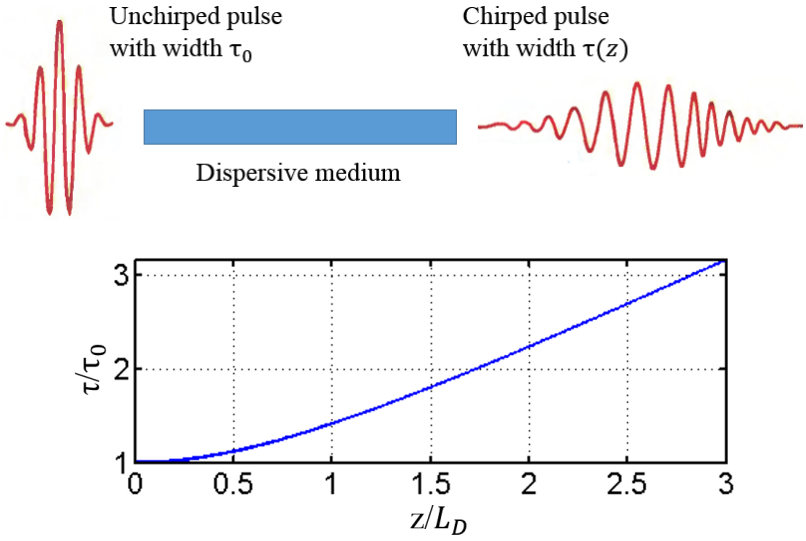

Figure 2.1 Propagation of a Gaussian pulse through a dispersive medium. Pulse width increases with increasing propagation distance z [1].

In the normal dispersion regime ($\beta_2 > 0$), lower frequency components (red) travel faster than the higher frequency components (blue). In contrast, the anomalous dispersion regime ($\beta_2 < 0$), blue travels faster than red. The type of chromatic dispersion depends on the material and the central frequency of the pulse.

The parameter β_3 in equation (2-10), which is the derivative of β_2, is referred to as the third order dispersion (TOD) coefficient. Although GVD dominates the pulse broadening, it is necessary to consider TOD if β_2 is small or the pulse is extremely short with a very broad spectrum [27]. Moreover, TOD also plays an important role in pulse shaping. For instance, the formation of an Airy pulse is a result of adding large TOD effect. Higher order dispersion terms in equation (2-10), which are not considered in this thesis, usually produce a negligibly weak effect on optical pulses.

For now, up to GVD term in equation (2-10) will be considered. Although ultrafast pulses have very short envelopes, they are still much longer than an optical cycle of the carrier frequency in most cases. In such case, the envelope of a pulse is approximately constant within one cycle ($\frac{\partial^2 A}{\partial t^2} \ll w_0^2 A$) and therefore $\frac{\partial^2 A}{\partial t^2}$ can be neglected in the wave equation; however, the GVD effect on the envelope is retained. The result is called the slowly varying envelope approximation (SVEA). By applying the SVEA to the wave equation, the envelope $A(z,t)$ satisfies the differential equation

$$j\frac{\partial A}{\partial z} - \frac{\beta_2}{2}\frac{\partial^2 A}{\partial t^2} = 0. \qquad (2\text{-}14)$$

This equation can be recognized as the diffusion equation.

Diffraction is another inherent property of optical waves. Similar to the pulse broadening in the time domain due to dispersion, diffraction effect spreads wave-front in

space. The propagation of a monochromatic beam with a complex envelope $A(x, y, z)$ is governed by the 2D paraxial wave equation

$$\nabla_T^2 A - j2k\frac{\partial A}{\partial z} = 0, \qquad (2\text{-}15)$$

where $\nabla_T^2 = (\frac{\partial^2}{\partial x^2} + \frac{\partial^2}{\partial y^2})$ and $k = \frac{w_0 n(w_0)}{c}$. The equation (2-25) is also derived from Helmholtz equation by SVEA ($\frac{\partial^2 A}{\partial z^2} \ll k_0^2 A$).

The Gaussian beam is a widely used solution of the 2D paraxial wave equation. Gaussian beams can be understood as a superposition of plane waves with different transverse wavevectors. As the result, the wave-front of Gaussian beams will be spread in space since plane waves propagate in different directions. The diffraction effect can be characterized by the parameter called diffraction length or Rayleigh range L_R

$$L_R = \frac{\pi w_0^2}{\lambda}, \qquad (2\text{-}16)$$

where w_0 is the initial beam width and λ is the wavelength. A shorter diffraction length corresponds to a larger diffraction effect. The Gaussian beam width *w* after propagation distance *z* is expressed as

$$w(z) = w_0\sqrt{1 + (\frac{z}{L_R})^2}. \quad (2\text{-}17)$$

From the above equation one can see that the beam width w increases from its initial minimum width w_0 as the beam propagates. After a propagation distance of one diffraction length ($z = L_R$), the Gaussian beam will spread by a factor of $\sqrt{2}$. The beam width will doubled at $z = \sqrt{3}L_R$.

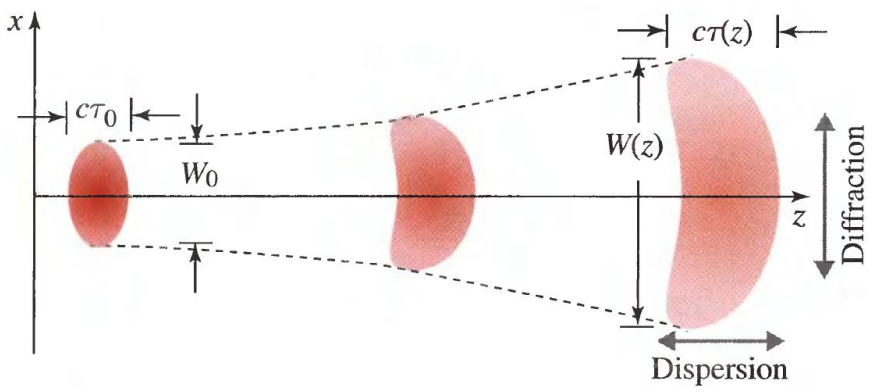

Figure 2.2 Spreading of a 3D spatio-temporal wave packet due to dispersion and diffraction [1].

Dispersion and diffraction have similar spreading effects on optical wave packets in the temporal and the spatial domain, respectively. Figure 2.2 illustrates the dispersion and diffraction spreading effect on a 3D wave packet that propagates in a dispersive medium.

2.3 Airy pulses

In the temporal domain, there is only one propagation-invariant solution of equation (2-14). Equation (2-18) shows the Airy pulse profile solution which is the non-dispersive solution to the SVE equation (2-14).

$$A(t,z) \propto Ai\left(t-\left(\frac{z}{2}\right)^2\right)\exp\left(j\left(\frac{tz}{2}-\frac{z^3}{12}\right)\right). \quad (2\text{-}18)$$

An Airy pulse can be generated by adding a TOD to a flat infinitely wide spectrum. But this is not physical since the ideal Airy pulse contains infinite energy. In experiment a truncated Airy pulse is formed by adding TOD to a wide spectrum such as a wide Gaussian spectrum. The truncated Airy pulse generation process is shown in equation (2-19) where $|\tilde{E}(w)|$ represents a broad spectrum and a represents the TOD.

$$\tilde{E}_{Airy}(w) \propto |\tilde{E}(w)| \cdot \exp(j \cdot aw^3) \quad (2\text{-}19)$$

Even though the truncated Airy pulses is not ideal, it is still non-dispersive for a long propagation distance. Figure 2.3 shows the simulated results for an Airy pulse (Figure 2.3(b)) generation by adding a large positive TOD (a) to a Fourier transform-limited (TL) Gaussian pulse (Figure 2.3(a)). The group delay $t_{gr}(w)$ is defined by the derivative of the spectral phase ($t_{gr}(w) = \frac{\phi(w)}{w}$) [28, 29]. Therefore, the cubic phase will delay (or lead) both shorter (blue) and longer (red) wavelength components while the central wavelength components correspond to the main lobe in Airy pulses.

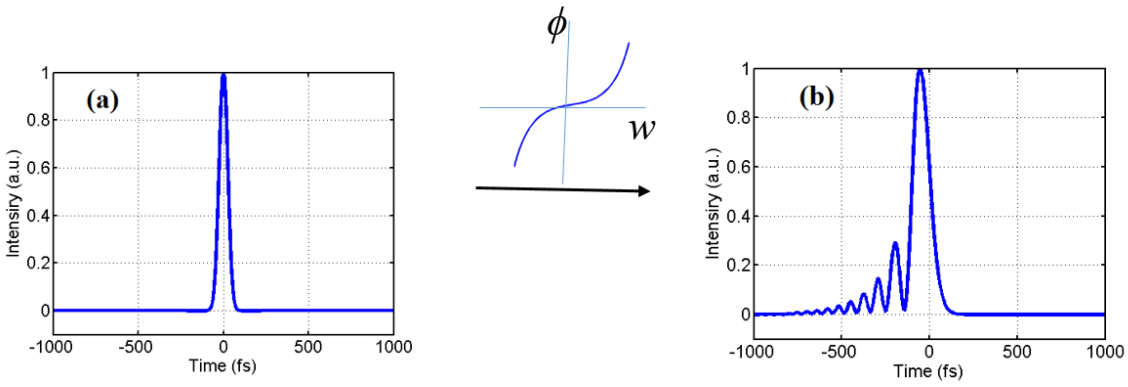

Figure 2.3 Simulated results for an Airy pulse (b) converted from a Gaussian pulse (a). a > 0.

In order to verify the non-dispersive and self-accelerating feature of Airy pulses, the evolution of an Airy pulse in a dispersive medium is calculated according to equation (2-14). The frequency domain solution of the equation (2-14) after the GVD of the medium is added is [30].

$$\tilde{E}(w) = |\tilde{E}(w)| \cdot \exp(j \cdot aw^3) \cdot \exp\left(j \cdot \frac{1}{2}\beta_2 w^2 z\right) \quad (2\text{-}20)$$

In equation (2-20), the first exponential term is the TOD on the initial Airy pulse while the second exponential term is the GVD accumulated during the pulse propagation in a dispersive medium. Equation (2-20) can be rewritten as

$$\tilde{E}(w) = |\tilde{E}(w)| \cdot \exp\left(j\left(a\left(w + \frac{\beta_2 z}{6a}\right)^3 - \frac{\beta_2^2 z}{12a}\left(w + \frac{\beta_2 z}{6a}\right) \cdot z\right)\right) \cdot \exp(jC). \quad (2\text{-}21)$$

The corresponding pulse, which is the Fourier transform of equation (2-21), is also an Airy pulse. In equation (2-21), the phase term includes a central frequency shift of $\left(w + \frac{\beta_2 z}{6a}\right)$, an extra linear phase and a constant phase term. The extra linear phase term leads to a temporal shift which is referred to as the self-acceleration. The self-acceleration exists for both normal ($\beta_2 > 0$) and anomalous dispersion ($\beta_2 < 0$) while the acceleration direction depends on the sign of the initial TOD. The central frequency is shifted by $\frac{\beta_2 z}{6a}$ but the magnitude of the shifted frequency is inversely proportional to the TOD (a). Therefore, a larger TOD on initial pulse is desired to enhance the pulse localization during propagation by reducing the central frequency shift. Figure 2.4 illustrates the dispersion-free propagation of an Airy pulse comparing to a Gaussian pulse when they propagate in a dispersive medium. While the temporal width of the Gaussian pulse is broadened significantly after a long propagation distance, the Airy pulse still maintains the initial main lobe width. Also, the peak intensity of the Airy pulse drops much slower than the Gaussian pulse. The simulation also shows the temporal shift of the Airy pulse which is the result of the self-acceleration feature.

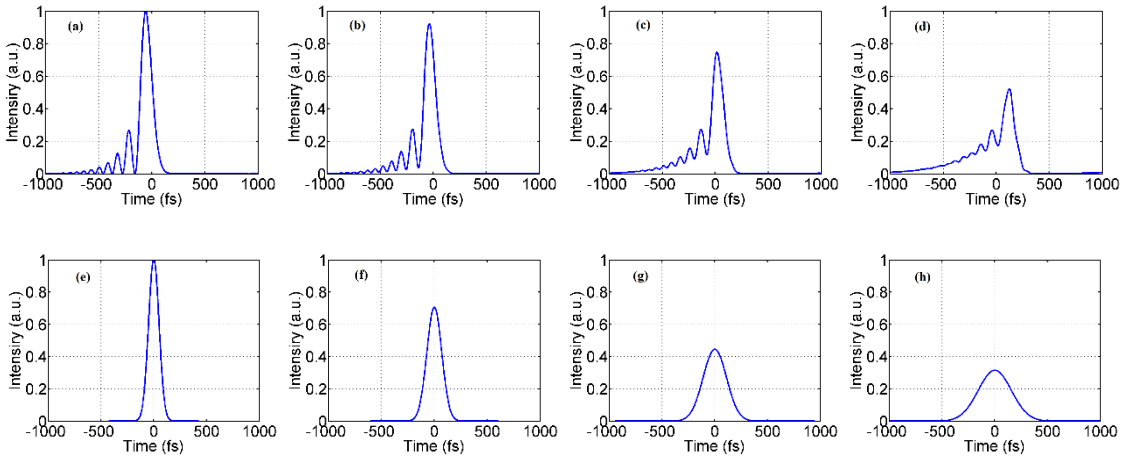

Figure 2.4 Simulated results for an Airy pulse and a Gaussian pulse propagating in a dispersive medium with normal dispersion. The Airy pulse after dispersive propagation through 0 (a), 1 (b), 2 (c), 3 (d) dispersion lengths (L_d). The initial Gaussian pulse after dispersive propagation through 0 (e), 1 (f), 2 (g), 3 (h) dispersion lengths (L_d).

2.4 Bessel beams

Among localized waves in the 2D spatial domain, a Bessel beam is the most well-known non-diffractive optical beam. In the spatial domain, diffraction-free beam profiles $E(x, y)$ satisfy 2D paraxial wave equation (2-15) [1]. The Bessel beam solutions of equation (2-15) are given by

$$E(x, y) = E_m J_m(k_r \rho) \exp(jm\phi), \mathrm{m} = 0, \pm 1, \pm 2, \ldots, \qquad (2\text{-}22)$$

where $J_m(\cdot)$ is the Bessel function of the mth order and k_r is the radial component of the wavevector.

The Bessel beam can be understood as a superposition of plane waves which have same amplitude and same wavevector projection on the propagation direction [31]. In the wavevector (spatial frequency) space, plane waves forming a Bessel beam have the same radial wavevector k_r while k_ϕ, which is the azimuthal wavevector, is again constant for all plane waves. Therefore, the wavevector on propagation axis k_z ($k_z^2 = k_0^2 - k_\phi^2 - k_r^2$) is again same for all plane waves. In such superposition, wavevectors of plane wave lay

on the surface of a cone. Such wavevector distribution leads to a stable transverse wave-front in propagation [19]. In addition, a Bessel beam has a self-healing property. If the part of the Bessel beam is blocked by an object, the beam regains its original Bessel function profile after some propagation distance [31]. Nowadays, Bessel beams are widely applied to optical manipulation [32] and plasma generation [33].

Unfortunately, it is not possible to generate ideal Bessel beams in since the ideal Bessel function contains infinite amount of energy. However, truncated Bessel beams still propagate without diffraction for a long propagation distance. The zeroth order Bessel beam can be generated conveniently by a conic lens which is called an axicon lens. Figure 2.5 shows the method to generate zero-order Bessel beams by illuminating a Gaussian beam on an axicon lens. In order to create higher-order Bessel beams that have phase singularity associated with the azimuthal phase term $\exp(jm\phi)$ (see equation (2-22)), initial illuminating beams with an azimuthal phase variation, such as Laguerre Gaussian (LG) beams, are required [34]. The azimuthal phase is conserved after the axicon Bessel beam transformation. Other methods to generate Bessel beams are holographic phase mask, spatial annular slits, etc.

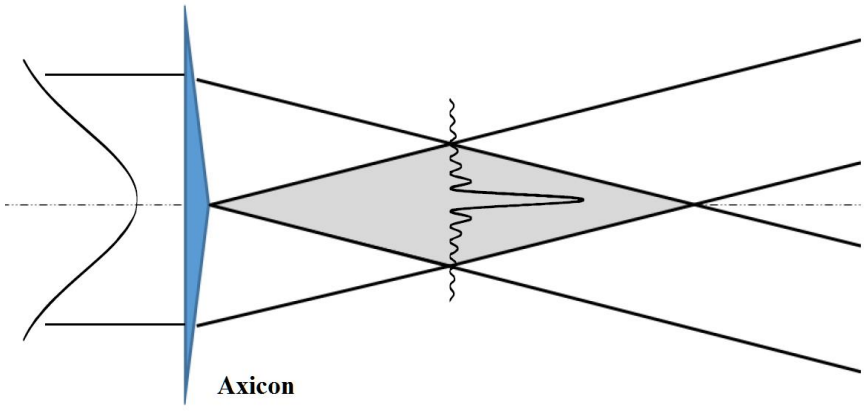

Figure 2.5 Generation of a zero-order Bessel beam using an axicon lens.

The simulated result of a zero-order Bessel beam generation by an axicon is shown in figure 2.6. It is generated by illuminating a 1mm Gaussian beam on an axicon lens. The simulated Bessel beam intensity profile (Figure 2.6 (a), (b)) has a central bright spot and several rings. There is π phase shift between adjacent rings shown in the transverse phase profile (Figure 2.6(c)). Distinguished from the zero-order Bessel beam, the higher-order Bessel beam has the azimuthal phase of $\exp(jm\phi)$.

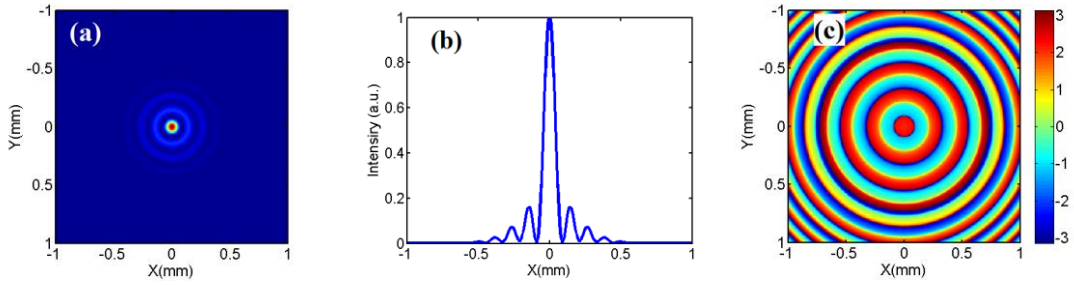

Figure 2.6 Simulated results for a zero-order Bessel beam generated by an appropriate axicon lens. The spatial beam profile (a), the normalized intensity profile along radial direction (b) and the transverse phase profile (c).

2.5 Optical vortices

Optical vortices are beams possessing optical angular momentum with an isolated central phase singularity. Today, optical vortices are not only an interesting research topic but also important tools for a variety of applications such as optical tweezers, free-space telecommunications, super-resolution optical microscopy, etc. [19].

A typical optical vortex beam can be presented by

$$E(r,\phi) = |E(r)|\exp(-jl\phi), \qquad (2\text{-}23)$$

where $|E(r)|$ is the spatial beam profile, which is a Gaussian profile in general, and l (integer) is referred to as the topological charge. A typical optical vortex beam is a Laguerre-Gaussian (LG) beam with an azimuthal phase. Figure 2.7 shows the LG modes with topological charges of $l = \pm 1$. In Figure 2.7, the right column illustrate the beam

intensity profiles which are LG beams. In the left column of Figure 2.7, the Poynting vector (green line), which indicates energy flow direction, has a spiral curve line resulting an orbital angular momentum in the propagation direction. LG vortex beams can be generated by the hologram (see Figure 2.8) using a spatial light modulator (SLM).

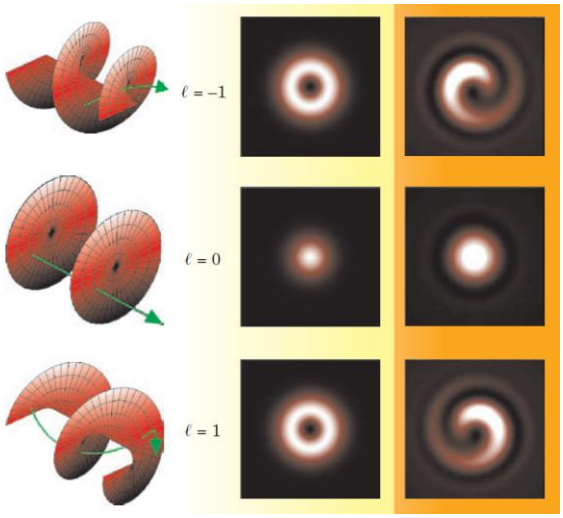

Figure 2.7 LG modes with different topological charges [19].

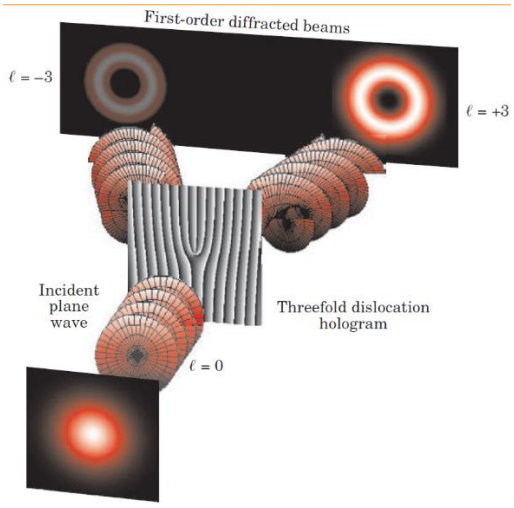

Figure 2.8 Generation of LG modes using a hologram mask [19].

2.6 Optical vortex Airy-Bessel wave packets

In previous sections, Airy pulses, Bessel beams and optical vortices have been discussed. In this section, the optical vortex Airy-Bessel wave packet is introduced. The combination of equation (2-14) and (2-15) leads to a generalized paraxial wave equation that describes the evolution of 3D spatio-temporal wave packets:

$$\frac{1}{2k}\nabla_T^2 A - \frac{\beta_2}{2}\frac{\partial^2 A}{\partial t^2} - i\frac{\partial A}{\partial z} = 0. \qquad (2\text{-}24)$$

The first term in equation (2-24) indicates the diffraction effect while the second term accounts for the GVD effect.

Equation (2-24) admits a propagation-invariant solution with a spatio-temporal intensity profile

$$E(r,z,\tau) = E_0 Ai\left[\pm\frac{\tau}{\tau_0} - \frac{(\beta_2^2 z^2)}{4\tau_0^4}\right] J_l\left(\frac{r}{r_0}\right)\exp(jl\phi), \qquad (2\text{-}25)$$

where E_0 is the peak amplitude while τ_0 and r_0 determine the temporal width and the beam width of the wave packet. $J_l(\cdot)$ and $Ai(\cdot)$ corresponds to the Bessel function and the Airy function while the ± sign in the Airy function indicates the orientation of Airy pulse which is determined by the sign of the initial TOD. The exponential term $\exp(jl\phi)$ is the azimuthal phase of the vortex while *l* is the topological charge. This solution is a non-varying spatio-temporal wave packet which is a combination of a non-dispersive Airy pulse and a non-diffractive higher order Bessel beam with a vortex profile. Since Airy pulses are non-dispersive and higher order Bessel beams are non-diffractive, the wave packet works as a linear light bullet that can propagate without spreading in any linear medium. Furthermore, the wave packet carries an orbital angular momentum. The principal of the vortex Airy-Bessel wave packet formation is shown in Figure 2.9. First, an azimuthal phase is applied to form a LG vortex beam. The LG vortex beam is converted into a higher order Bessel beam.

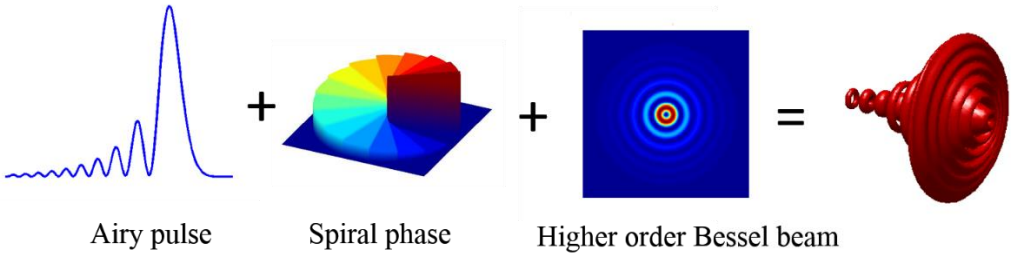

Figure 2.9 Formation of the vortex Airy-Bessel wave packet.

2.7 Collisions between vortices in both the spatial and the temporal domains

A vortex beam possesses an optical angular momentum in the direction of propagation. Studying the interactions between optical beams carrying angular momentums is an interesting scientific topic.

Controlled collisions between vortex beams were reported by Rosales-Guzman *et al.* [24]. In the vortex collision study, vortices are embedded in two counter-accelerating Airy beams. The embedded vortices collide in space since two Airy beams accelerate toward each other to eventually overlap two phase singularities [24]. Interestingly, the repulsion effect between the phase singularities has been observed when vortices with the same topological charge are overlapped. In contrast, the collision between vortices with opposite topological charges exhibit the attraction between singularities. When two singularities are overlapped, the annihilation of phase singularities occurs. Figure 2.10 and 2.11 show the measurement of the spatial collision between two Airy vortex beams from ref. [24]. In Figure 2.10, phase singularities cannot be overlapped perfectly. In fact, phase singularities are getting further away when vortices have the same topological charge. This can be explained as the repulsion between same orbital angular momentums. In contrast, Figure 2.11 shows the attraction and the annihilation between vortices with opposite topological charges. This can be explained as the attraction of the opposite sign orbital angular momentums.

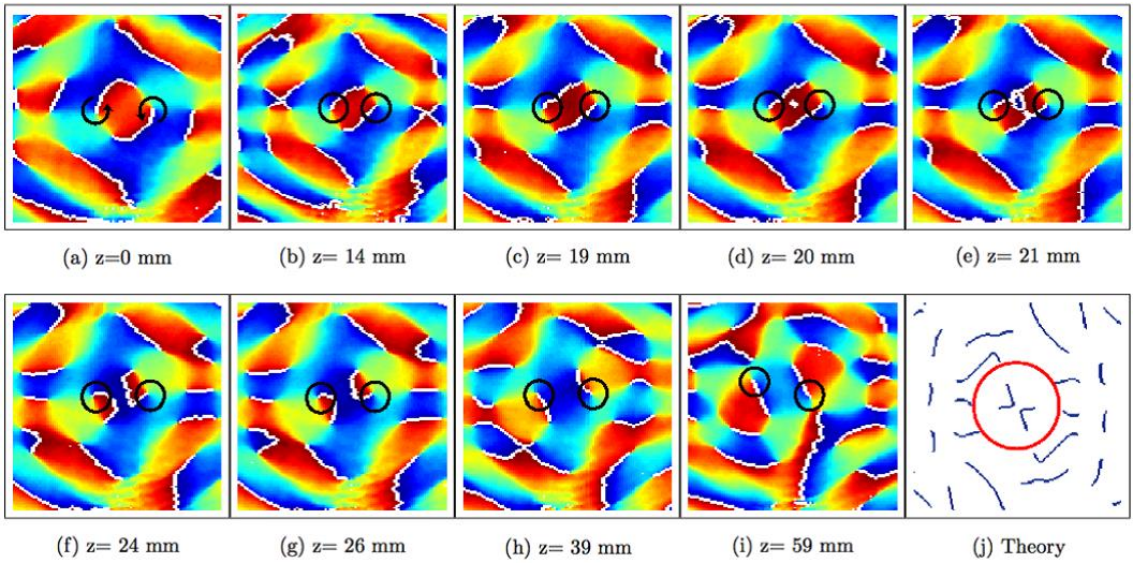

Figure 2.10 Interactions of spatially colliding vortex Airy beams with same topological charges when propagating along *z* axis. Circles represent phase singularities [24].

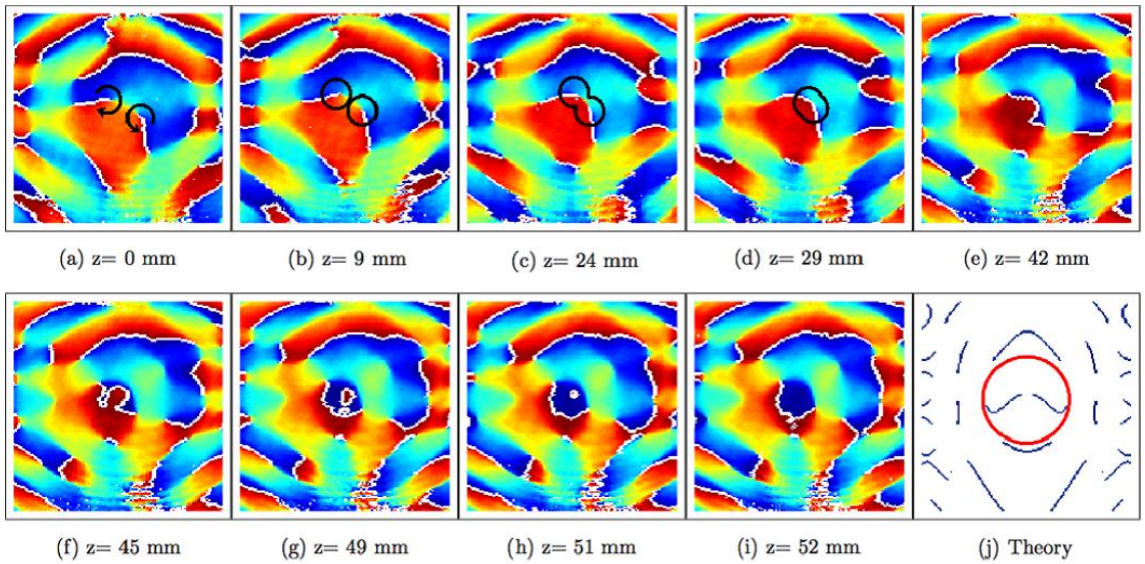

Figure 2.11 Interactions of spatially colliding vortex Airy beams with opposite topological charges when propagating along *z* axis. Circles represent phase singularities [24].

In the following, the study of the controlled collision between vortex wave packets in the temporal domain is shown. The numerical simulation of the collision between two vortex spatio-temporal wave packets in time is shown in Figure 2.12. One wave packet contains a vortex beam with an accelerating Airy pulse profile in the temporal domain while the other wave packet beam consists of a vortex beam with a

Gaussian pulse. Since the Airy pulse will accelerate to capture and collide the Gaussian pulse, controlled collisions between vortex wave packets in temporal domain can be accomplished. For the same unitary topological charge case ($l = 1$), the transverse intensity profile in the collision region is a vortex beam itself (figure 2.12 (b)). However, a new beam profile (a Hermite Gaussian beam without an azimuthal phase) appears by colliding vortex with opposite topological charges (figure 2.12 (c)). As the result, the overlapped wave packets has a topological charge as a function of time. The transverse beam profile outside the interaction region has the topological charge of 1 while the beam profile in the temporally overlapped region has the topological charge of 0.

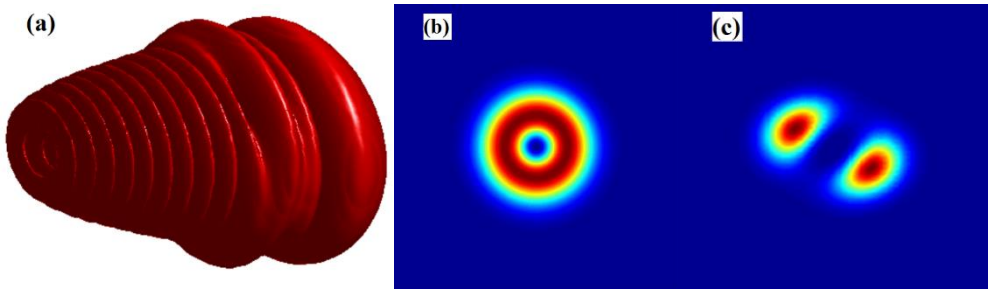

Figure 2.12 Simulated 3D collision between a vortex Gaussian-LG wave packet and a vortex Airy-LG wave packet with same and opposite unitary topological charges. The 3D iso-intensity profile (a) and the intensity profile on the collision transverse plane in the same (b) and opposite (c) unitary topological charge case.

Similar to the spatial vortex collision, the attraction (repulsion) effect is expected between vortices with opposite (same) topological charges during collisions in the temporal domain. Our initial expectation was that when two vortex wave packets collide with a small transverse misalignment, phase singularities will move with respect each other due to the repulsion or attraction effect. Unfortunately, numerical simulations did not show the expected behaviors. Based on the simulated transverse intensity (the middle row in figure 2.13) and phase profiles (the last row figure 2.13), there is no attraction that

appears between singularities carrying opposite vortices. The same conclusion was obtained in simulation for the collision between vortices with the same charge.

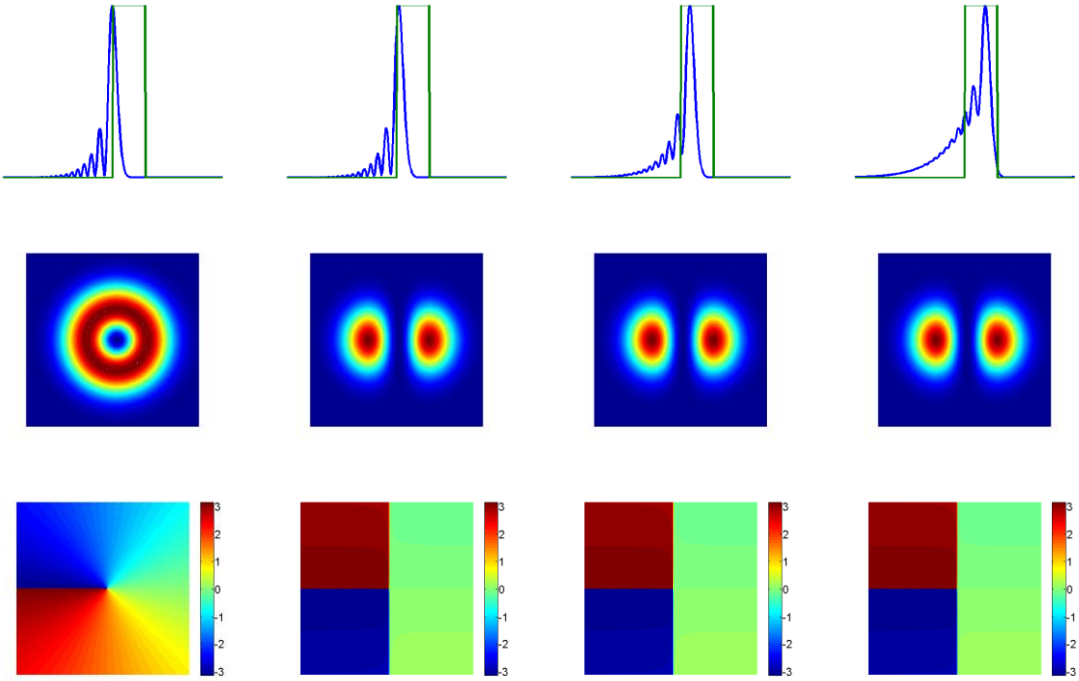

Figure 2.13 Collisions with a little transverse misalignment between two wave packets carrying vortices with opposite unitary charges. The Airy pulse accelerates to collide a rectangular pulse. The first row represents the pulse collision profiles in the time domain. The middle row represents the transverse intensity profiles in the collision regime. The last row represents the transverse phase profiles in the collision regime.

Even though the simulation result did not show clear interactions between vortices, it is believed that the numerical simulation is not sufficient to claim there won't be anything interesting in real experiments. Simulations are performed with a small number of parameter sets and there may be optimal conditions, which can be tried easily in the experiment, to observe the vortex interaction effect clearly. Therefore, we believe that it is worthy to investigate the vortex collision in the temporal domain in real experiments.

CHAPTER III

EXPERIMENTAL SYSTEM

In the previous chapter, theories of vortex Airy-Bessel wave packets and the time domain vortex collision are presented. In this chapter, the experimental systems, which include pulse duration characterization, spatio-temporal wave packet shaping method (pulse shaping & beam shaping) and 3D wave packet characterization method, are covered.

3.1 Pulse characterization

It is essential to characterize pulses in ultrafast optics experiments [1]. However, ultrafast pulse measurement is challenging since detectors are too slow to measure femtosecond scale pulses. A typical strategy to overcome this problem is to use the ultrashort pulse to sample itself to create an overlap in time between two identical pulses. A simple setup to achieve this is a Michelson interferometer. The average power emerging from the interferometer is a correlation function of a time delay (τ) between two pulses which provides an indirect information of the pulse duration. This method is called an electric field auto-correlation (AC) [28].

However, this linear technique is not able to determine the pulse when the pulse is chirped [28, 29]. In order to realize a more useful pulse measurement, a nonlinear effect is introduced in the Michelson interferometer. Typically a second harmonic generation (SHG), where the generated light has twice the frequency ($2w_0$) of the input light (w_0), is

introduced in the Michelson interferometer. The intensity of the SHG signal is proportional to the intensity square of the input light field. By generating the SHG signal of overlapped pulses with a time delay between them, detector records the time-averaged intensity square signal of overlapped pulses as a function of time delay τ. This measurement technique, which called an intensity AC, will provide a signal with correct pulse duration information regardless of the chirp on the pulse. By having collinear overlapping of pulses in the intensity AC, an interferometric AC can be obtained (Figure 3.1). The input pulse is split into two identical pulses, which are then recombined with time delay τ. Two pulses are collinearly overlapped and focused into a SHG crystal; the SHG signal will exhibit strong interference fringes as a function of a time delay. A high pass filter is set to select the SHG signal only [28]. In our experiment, the auto-correlator is constructed using a two-photon absorption detector with a large bandgap instead of a SHG crystal.

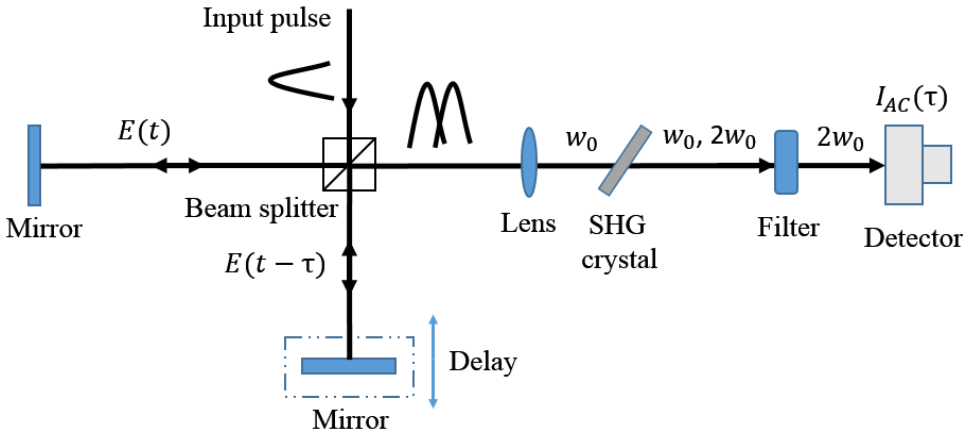

Figure 3.1 The setup for measuring interferometric AC for collinear SHG geometry.

The incident electric field on the SHG crystal is given by

$$E_{out}(t) = E(t) + E(t+\tau), \quad (3\text{-}1)$$

where $E(t)$ presents the object pulse and $E(t+\tau)$ is the reference pulse with certain delay τ. The field at SH frequency, which is proportional to the intensity of input electric field, can be written as

$$E_{SHG}(t) \sim |E_{out}(t)|^2 \sim |\mathrm{E}(t) + E(t+\tau)|^2. \quad (3\text{-}2)$$

The AC signal is recorded by a detector, where the photocurrent is proportional to the interferometric AC intensity function

$$I_{AC}(\tau) \sim \int (|E(t) + E(t+\tau)|^2)^2 dt. \quad (3\text{-}3)$$

Assuming a Gaussian pulse with temporal width τ_0 ($E(t) = e^{-\frac{t^2}{2\tau_0^2}} e^{jw_0 t}$), the interferometric AC signal is given by the following equation.

$$I_{AC}(\tau) = C \cdot \left(1 + e^{-\frac{1\tau^2}{2\tau_0^2}} + 4\cos(w_0\tau) \cdot e^{-\frac{3\tau^2}{8\tau_0^2}} + 2cos^2(w_0\tau) \cdot e^{-\frac{1\tau^2}{2\tau_0^2}}\right) \quad (3\text{-}4)$$

The interferometric AC function is composed of following four terms: the first term in equation (3-4) is the background signal; the second term is the intensity AC; the third and fourth terms represent the oscillation with intensity AC envelop at frequency w_0 and $2w_0$ due to the interference.

Mathematically, equation (3-4) is a $sech^2$ function [28]. Figure 3.2 shows the simulated interferometric AC function with 40 femtosecond full width half maximum (FWHM) pulse duration of a Gaussian pulse at 1030 nm wavelength. Note that the maximum signal is the result of the perfect construction interference between two pulses. Since perfectly overlapped pulses have two times higher amplitude than a single pulse, sixteen times higher SHG signal over the background will be recorded by the detector (equation (3-3)). For a large delay, two pulses do not overlap and therefore the SHG signal is only two times over the background. Therefore, the AC signal shows 1 to 8

contrast rate as shown in Figure 3.2. Also for a Gaussian pulse, there is a linear relationship ($\tau_{AC}^{FWHM} = 1.53 \cdot \tau_{pulse}^{FWHM}$) between the FWHM of the AC signal and the real pulse duration. The pulse duration can be calculated indirectly from the FWHM of the AC signal.

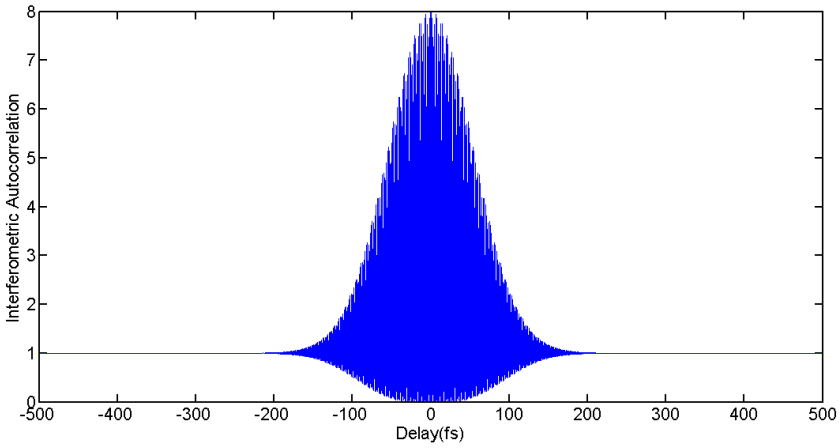

Figure 3.2 Simulation of an interferometric AC signal.

Apart from the AC technique, a cross-correlation (XC) can also be measured. The XC signal is generated by overlapping an unknown pulse with a known pulse which can be substantially different from the unknown pulse. In general, XC is used to characterize unknown pulses by correlating with substantially shorter known pulses. We refer the pulse to be measured as the object or signal pulse while the known shorter pulse is referred as the reference pulse. When the reference pulse is much shorter than the object pulse, the reference can be approximated as a delta function. Therefore, the recorded signal directly gives the intensity profile of the object pulse [28].

3.2 Pulse shaping

The pulse shaping is a technique to control the temporal profile of pulses. It is typically based on the phase or amplitude modulation of a pulse by the frequency filtering

in the spectral domain. The filters in the spectral domain can be programmable masks or spatial light modulators (SLM). The general setup for the pulse shaping with a SLM is shown in Figure 3.3. The first grating and a lens spreads the spectrum and collimates in space. By inserting a programmable modulator at the focal plane which is the spectral plane, each spectral components can be controlled by a modulator. After the spectrum is modified, spectral components are recombined by another grating.

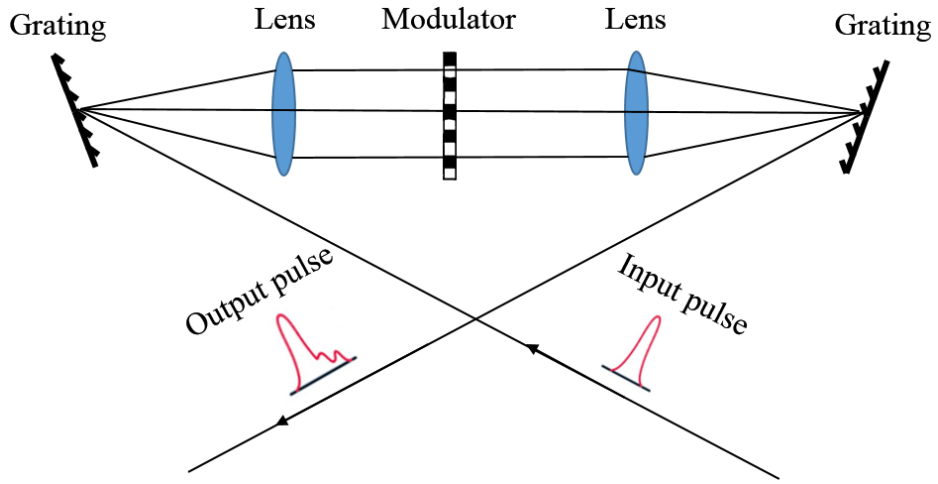

Figure 3.3 General setup for modulator based pulse shaping.

Mathametically, an input pulse denoted by $e_{in}(t)$ and $E_{in}(w)$ in the time and the frequency domain repectively, passes though a pulse shaper with spatial mask $M(x)$. $e_{in}(t)$, $E_{in}(w)$ and $M(x)$ are complex functions representing the amplitude and phase profiles of the input pulse and the spatial mask. The output pulse is the spectrum of the input pulse multiplied by the complex frequency response function which corresponds to the spatial mask function of the modulator

$$E_{out}(w) = E_{in}(w) \cdot M(\alpha w). \qquad (3\text{-}5)$$

α presents the spatial resolution at the modulator plane ($\alpha = \frac{x}{w} = \frac{dx}{dw}$). The output pulse in time is obtained by the inverse Fourier transfrom of equation (3-5)

$$e_{out}(t) = e_{in}(t) * m(t/\alpha), \qquad (3\text{-}6)$$

where

$$m(t/\alpha) = \frac{1}{2\pi}\int M(\alpha w)e^{jwt}dw. \qquad (3\text{-}7)$$

The output pulse can be presented by the input pulse convolved with the impulse response function ($m(t/\alpha)$) [35].

In this experiment, a programmable liquid-crystal (LC) SLM is chosen to serve as the modulator at the spectral plane. A SLM is an electrically programmable device that modulates light based on numerous spatial pixels. Figure 3.4 illustrates the general layout of a single layer SLM which can be used for the phase modulation. A SLM with double layers for both phase and amplitude modulation will be discussed later.

The single layer SLM consists of a piece of nematic liquid crystal material sandwiched between two glass plates. Conducting films (such as indium tin oxide (ITO)) are coated on the inside surface of each glass plate. Numerous separate electrodes (or pixels) that correspond to applied electric field (or applied voltage) are patterned on a piece of a confucting film. The conducting film on the other glass plate is unpatterned and serves as a groud plane. The nematic liquid crystal which consists of numerous long, thin and rod-like unit molecules is located in between glass plates. For each single electode (or pixel) region, in the absence of electric field, the molecules are perfectly alingned along y axis shown in Figure 3.5(a). The beam propagating in the direction of *z* axis will experience two differenct refractive indexes: the light polarized along *y* axis (parallel to long axe of the molecules) will experience a larger refactive index while the light polarized along *x* aixs will face a smaller index of refraction. As a result, there will be phase diffrence between two orthogonal polariations due to birefringence. When an

electric filed is applied, molecules will be tilted to point into z axis (Figure 3.5 (b)) resulting less birefringence effect. The tilted angle depends on the amplitude of the applied electric field. As a result, the phase shift can be controlled by the amount of applied voltage. The phase difference between two polarization $\Delta\Phi(V)$ can be controlled as a voltage-dependent birefringence.

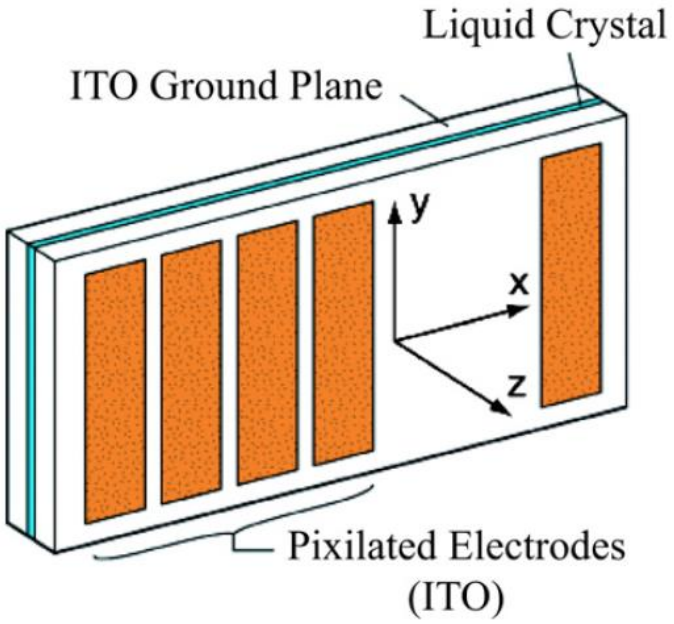

Figure 3.4 Basic layout of SLM with single layer used for pulse shaping [35].

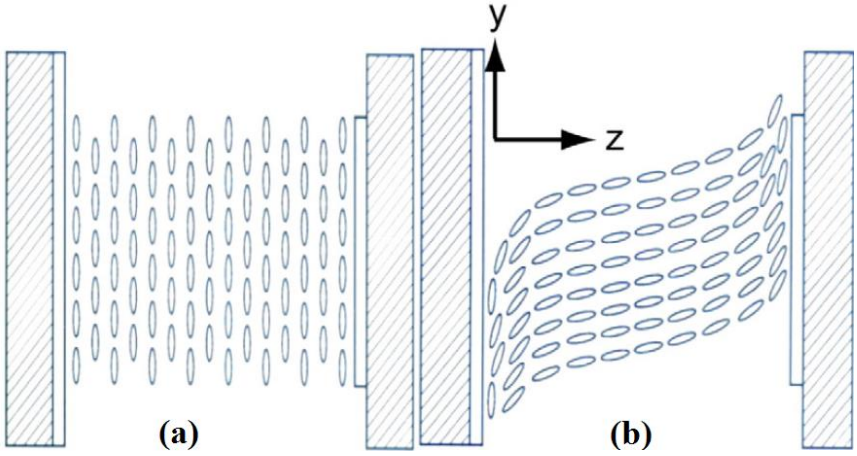

Figure 3.5 Side view of a liquid crystal pixel. (a) No applied electric field. (b) Electric field applied in the propagation direction (z axis) [35].

In order to control phase and amplitude modulation independently, a two-layer SLM is required. A two-layer SLM has two pieces of nematic liquid crystal material, which are aligned at 45 degree and -45 degree with respect to x axis, respectively. Applied voltage tilts the molecules in each pixel towards *z* axis and results in phase modulation for the light components whose polarization is parallel to the long axix of molecules. Mathematically, the operation can be expressed in terms of components along ±45 degrees directions:

$$\begin{pmatrix} E_{x'}^{out} \\ E_{y'}^{out} \end{pmatrix} = \frac{1}{\sqrt{2}} \begin{pmatrix} e^{j\Delta\Phi_1(V_1)} & 0 \\ 0 & 1 \end{pmatrix} \begin{pmatrix} 1 & 0 \\ 0 & e^{j\Delta\Phi_2(V_2)} \end{pmatrix} \begin{pmatrix} E_x^{in} + E_y^{in} \\ E_y^{in} - E_x^{in} \end{pmatrix}. \quad (3\text{-}8)$$

where $E_{x'}^{out}$ and $E_{y'}^{out}$ represent the output electric field components along new x and y directions, respectively, while E_x^{in} and E_y^{in} represent the input electric field components along original x and y directions, respectively. $\Delta\Phi_1(V_1)$ and $\Delta\Phi_2(V_2)$ represent the voltage-dependent birefringence of two layers, respectively. In the case where the input electric field and the output polarizer are both oriented along y axis, the output electric field is given as

$$E_{out} = E_{in}\exp\left(j\frac{1}{2}(\Delta\Phi_1(V_1) + \Delta\Phi_2(V_2))\right) \cdot \cos\left(\frac{1}{2}(\Delta\Phi_1(V_1) - \Delta\Phi_2(V_2))\right). \quad (3\text{-}9)$$

From equation (3-9), we can see that the amplitude modulation depends on the difference of birefringences while the phase modulation depends on the summation of two birefrigences. Therefore, by determining $\Delta\Phi_1(V_1)$ and $\Delta\Phi_2(V_2)$, one can controll the amplitude and the phase indenpendently [35].

3.3 Beam shaping

Apart from the pulse shaping in time domain, a SLM can also be used to shape spatial beam profiles. The beam shaping, which is done by a spatial phase mask is more

straightforward than the pulse shaping. As a monochromatic beam denoted by $E_{in}(x, y)$ passes though a modulator with a spatial mask $M(x, y)$, the corresponding output beam profile is just the input beam profile multiplied by a complex spatial mask function

$$E_{out}(x, y) = E_{out}(x, y) \cdot M(x, y). \qquad (3\text{-}10)$$

Figure 3.6 shows a typical setup for the beam shaping using a SLM. The SLM modulated wave-front transfroms into a controlled diffraction pattern in the far field. For instance, when a helical phase mask is applied on a SLM, the output beam becomes a vortex beam in the far field.

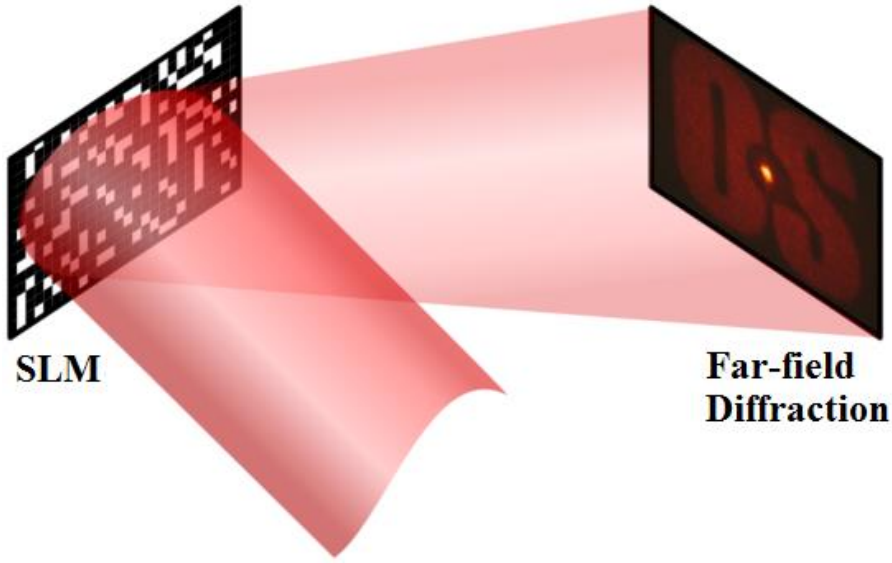

Figure 3.6 Conceptual setup for real space beam shaping using SLM [36].

Since the vortex Airy-Bessel wave packet has separable temporal and spatial profile, it can be created by performing the pulse shaping and the beam shaping separately in series.

3.4 Three-dimensional measurement method

As discussed previously, pulses can be characterized based on the correlation technique. For the spatial profile measurement, a charge-coupled device (CCD) camera

is commonly used. Separate characterization of pulses and beams are sufficient for most wave packets. However, separate temporal and spatial diagnostic cannot give the full information about the wave packet if it has a spatio-temporally coupled profile. In such case, an appropriate 3D measurement system is required. We adopted a simple wave packet measurement system suggested by Li *et al.* to measure the wave packet intensity profiles in 3D, which is based on the first order XC detected by a CCD camera [37].

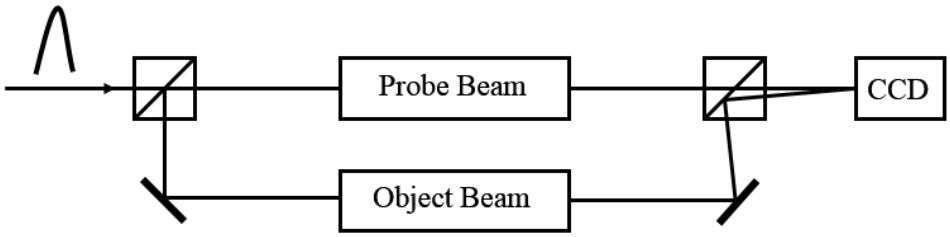

Figure 3.7 Conceptual setup for 3D measurement system.

The schematic of the 3D measurement system suggested by Li *et al.* is illustrated in Figure 3.7 [38]. The initial wave packet is split into two beam paths. One serves as a probe wave packet while the other beam path serves as the object wave packet after the pulse and beam shaping. A probe and an object beam are finally recombined with an adjustable delay on a CCD camera at a small tilted angle. The angle between the two beams should be carefully chosen in order to generate an appropriate interference fringe period which can be resolvable by the CCD camera pixel size. The CCD camera records the spatial intensity pattern as a function of delay τ between two pulses, which can be mathematically expressed by [38]

$$I_{CCD}(\vec{r},\tau) = \int dt\Big|A_o(\vec{r},t)\exp\big[i\phi_o(t) + i\vec{k}_o\cdot\vec{r} - iw_0t\big] + A_p(\vec{r},t-\tau)\exp\big[i\phi_p(t-\tau) + i\vec{k}_p\cdot\vec{r} - iw_0(t-\tau)\big]\Big|^2$$

$$= I_o(\vec{r}) + I_p(\vec{r}) + 2\cos\{w[\tau+\delta(\vec{r})]\} \times \int dt A_o(\vec{r},t)A_p^*[\vec{r},t-\delta(\vec{r})-\tau] \times \cos\big\{\phi_o(t) - \phi_p[t-\delta(\vec{r})-\tau]\big\}. \qquad (3\text{-}11)$$

Where $A(\vec{r},t)$ and $\phi(\vec{r},t)$ represent the 3D amplitude and the 3D phase of the wave packet. The subscripts o and p denote the object and the probe wave packets, respectively. $I_o(\vec{r})$ and $I_p(\vec{r})$ are the intensities of the object and the probe beam, respectively. $\delta(\vec{r})$ represents the temporal shift due to the angle between two pulses.

The probe pulse can be approximated as a δ function since it is much shorter than the object pulse. After the approximation is applied, equation (3-11) can be reduced to the following equation

$$I_{CCD}(\vec{r},\tau) \sim I_o(\vec{r}) + I_p(\vec{r}) + 2\cos\{w[\tau+\delta(\vec{r})]\} \times \sqrt{\Delta t_p i_o(\vec{r},\tau)}\sqrt{I_p(\vec{r})}. \qquad (3\text{-}12)$$

In equation (3-12), Δt_p represents the duration of the probe pulse and $i_o(r,\tau)$ is the object wave packet intensity as a function of time delays. Therefore, the 3D intensity of the object wave packet can be retrieved from

$$i_o(\vec{r},\tau) \sim C^2(\vec{r},\tau)/I_p(\vec{r}), \qquad (3\text{-}13)$$

where $C(\vec{r},\tau)$ is the amplitude of the coupling term in equation (3-12). It is obtained by subtracting the background signal from the original signal on the CCD camera and filtering out the cosine term. In other words, the coupling term corresponds to the spatial modulation depth of the interference pattern at different time delays.

According to equation (3-13), in order to determine the 3D intensity profile of the object wave packet, the intensities of probe beam and interference patterns at each time

delay are measured. Meanwhile, there are several points we need to consider. First, a proper angle between the beams should be chosen to obtain a fine spatial interference pattern. Second, a low-pass filter is required to smooth the envelope of spatial modulated depths in the data processing. Third, in order to achieve accurate measurements, a small temporal delay step size is desired in the measurement.

CHAPTER IV

EXPERIMENTAL RESULTS

In previous chapters, the theoretical background of the vortex Airy-Bessel wave packet and the experiment system are discussed. In this chapter, the 3D measurement of the linear propagation dynamics of the vortex Airy-Bessel wave packet will be presented. Moreover, the 3D measurement system for controlled vortex collisions in the temporal domain will also be discussed.

4.1 Experimental setup for the vortex Airy-Bessel wave packet

The experimental setup is shown in Figure 4.1, which is very close to the setup in Ref. [39]. From a mode-locked fiber laser oscillator, chirped picosecond pulses are generated and divided into two beam paths. A grating pair is set to compress the initial chirped pulse into a Fourier transform-limited (TL) femtosecond pulse, which serves as the probe wave packet (the lower path in Figure 4.1). Its temporal profile can be characterized with the auto-correlator. Another beam path serves as the object wave packet (the higher path in Figure 4.1). A cubic spectral phase is added to the object wave packet by the SLM to transform the initial Gaussian pulse into an Airy pulse in the pulse shaper setup. Its Airy temporal profile can be characterized by cross-correlating with the TL femtosecond probe pulse. After the Airy pulse is established, another SLM is implemented to apply a spiral phase mask to convert the initial Gaussian beam into a LG

vortex beam with a topological charge of 1. Lastly, an axicon lens converts a LG vortex beam into a higher order vortex Bessel beam [34].

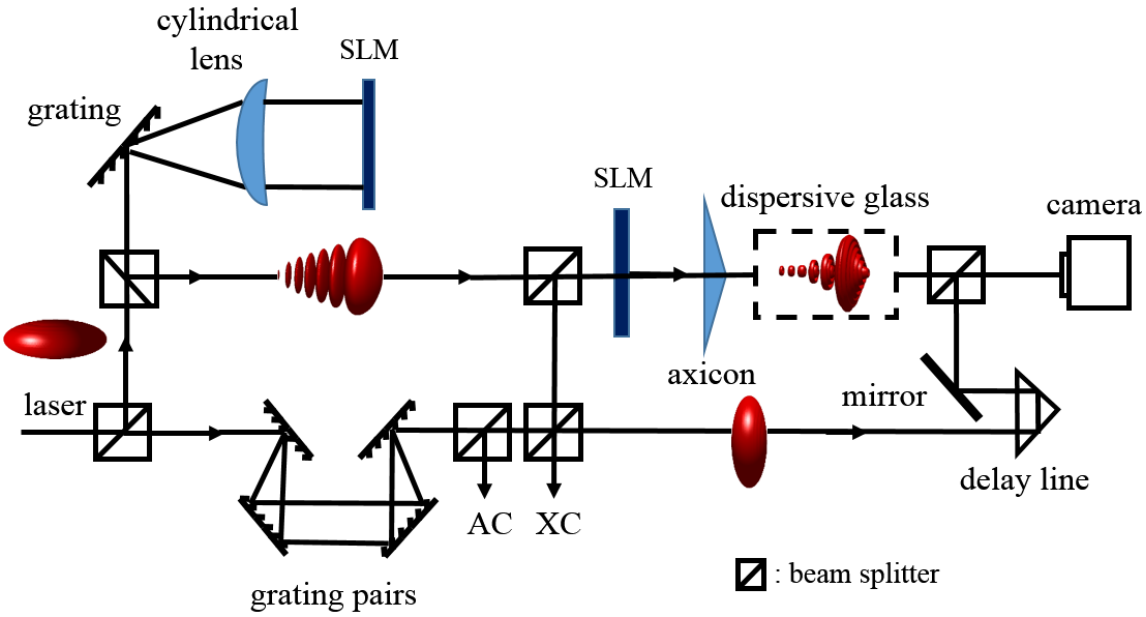

Figure 4.1 Experimental setup to generate and measure vortex Airy-Bessel wave packets.

The 3D measurement is performed by overlapping an object wave packet with a time-delayed probe wave packet in a small tilted angle on a CCD camera. In order to verify the non-varying feature of the vortex Airy-Bessel wave packet in linear propagation, a 3D measurement is performed after inserting a 4-inch-long-SF11 glass rod, which is highly dispersive and diffractive, in the object wave packet path.

4.2 Experimental results for linear propagation dynamics of vortex Airy-Bessel wave packets

The experimental pulse source is a femtosecond mode-locked fiber laser. The laser spectrum is showed in Figure 4.2 (a) which has nearly 70 nm bandwidth (BW) with the central wavelength of 1030 nm. The laser output power is ~ 70 mW with a repetition rate of 43 MHz. The beam profile is a fundamental Gaussian with the beam size of 1mm in diameter. The AC signal in figure 4.2 (b) shows that the laser output pulse has 60 fs

FWHM pulse duration after compressed by a grating pair. The object Airy pulse profile is measured in XC by correlating the object pulse with the 60 fs TL pulse. The XC signal, which clearly shows the Airy pulse features, is presented in Figure 4.2 (c). The main lobe of the XC signal has 146 fs width in FWHM which corresponds to 119 fs main lobe pulse duration of the Airy pulse.

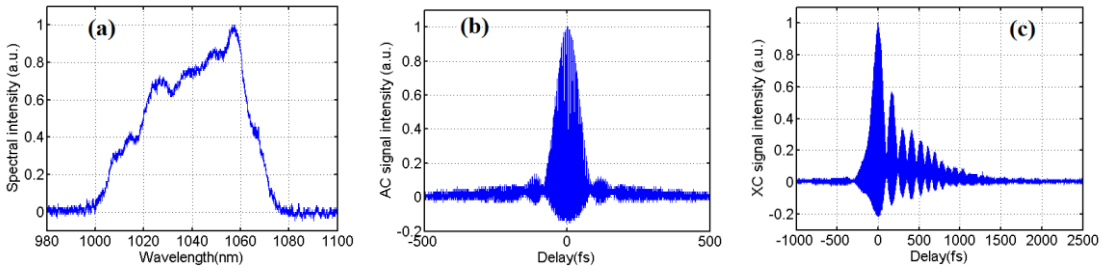

Figure 4.2 The characteristics of the fiber laser. The measured spectrum (a), the AC signal between transform-limited probe pulses (b) and the XC signal between the Airy pulse and the probe pulse (c).

3D measurement results for the vortex Airy-Bessel wave packet are presented in Figure 4.3 (d)-(f) while the simulation results are also shown in Figure 4.3 (a)-(c). Figure 4.1 (a) and (d) show the iso-intensity 3D profiles of simulated and measured. The sagittal intensity profiles (Figure 4.3 (b), (e)) show the radial intensity profiles of the wave packet. The Airy pulse main lobe duration measured by the 3D measurement is 135 fs , which is very close to the measured result (146 fs) from the XC signal. The measured radial intensity distribution along the radial (y) axis shows the multiple ring structure of a higher-order Bessel beam with the central ring size of 194 um in diameter. The spiral phase structure is verified by the transverse phase measurement results (Figure 4.3 (c), (f)). The transverse phase measurement shows the π phase shift between the adjacent rings with a phase singularity at the center as expected for a vortex Bessel beam.

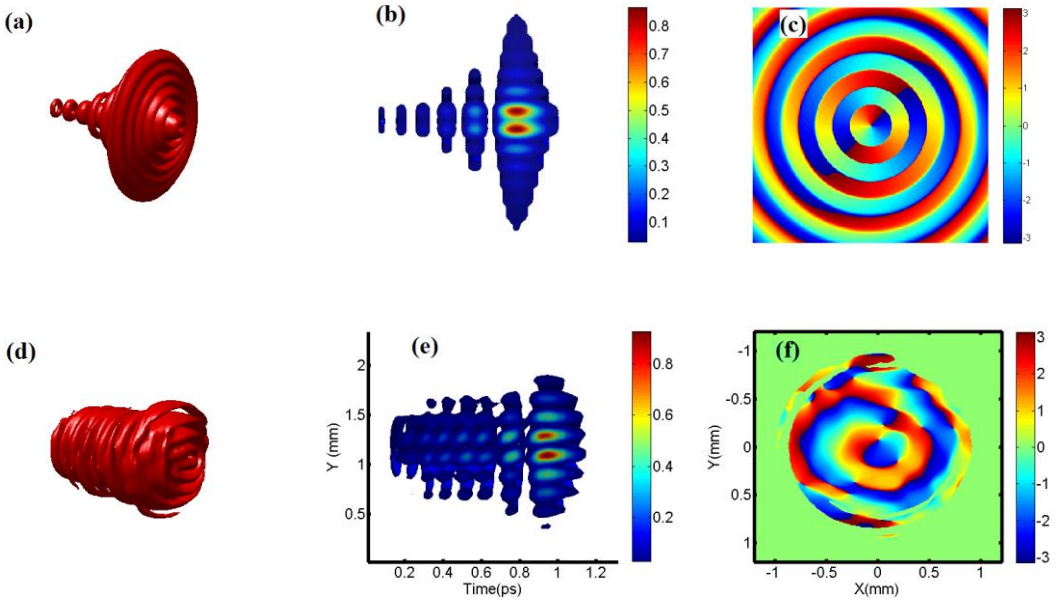

Figure 4.3. Simulation and 3D measurement results of the vortex Airy-Bessel wave packet without the glass rod. The simulated 3D iso-intensity profile (a), sagittal intensity profile (b) and transverse phase profile (c). The measured 3D iso-intensity profile (d), the sagittal intensity profile (e) and the transverse phase profile (f) [40].

In order to demonstrate the non-varying propagation of the vortex Airy-Bessel wave packet in a linear medium, 3D measurements have been obtained before and after inserting a highly dispersive material in the object path. In this experiment, a 4-inch-long SF11 glass rod is chosen. In theory, the wave packet experiences significant dispersion effect of ~2.5 L_D after passing through the glass rod. Theoretically, this dispersion effect is able to broaden a Gaussian pulse with the pulse duration of the Airy pulse main lobe duration by a factor of ~2.7 (see figure 4.4 (a), (b)). By inserting the glass rod, it also provides a significant diffraction effect to spread out the central ring beam by a factor of ~2 in diameter (see figure 4.4 (c), (d)).

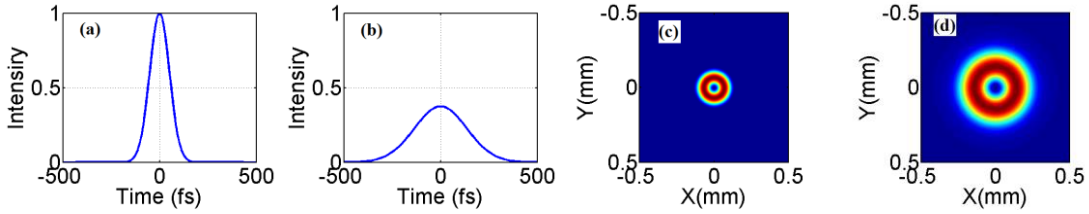

Figure 4.4. Dispersion and diffraction effects from the glass rod. Dispersion-induced broadening effect transforms the initial Gaussian pulse (a) into (b). Diffraction-induced spreading effect converts the initial ring beam (c) into (d).

The 3D measured results of the wave packet before and after propagating through the glass rod are shown in Figure 4.5. Despite the presence of a medium with significant diffraction and dispersion effects, the measurement (Figure 4.5 (e), (f)) reveals that the vortex Airy-Bessel wave packet maintained the 3D profile after passing through the glass rod. After the glass rod, the measured main lobe pulse duration of the wave packet is 147 fs which is not much different from 135 fs which is the initial input main lobe pulse duration. The central ring diameter of the Bessel beam is 211 um which again is not so much different from the initial ring diameter size of 194 um. The transverse phase profile (Figure 4.5 (f)) is also maintained with a singularity at the center.

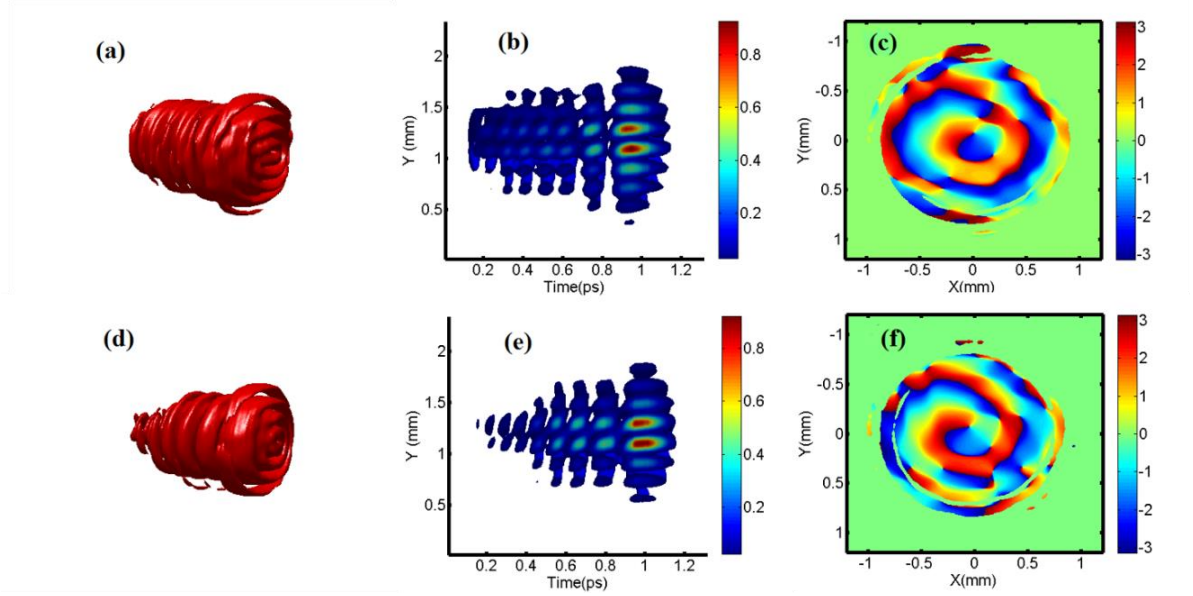

Figure 4.5. The 3D measurements of the vortex Airy-Bessel wave packet. The iso-intensity profiles (a) without and (d) with the glass rod. The sagittal intensity profiles (b) without and (e) with the glass. The transverse phase profiles (c) without and (f) with the glass rod [40].

The experiment demonstrates that the vortex Airy-Bessel wave packet is able to maintain its localization even under significant dispersion and diffraction effect. Therefore, the vortex Airy-Bessel wave packet is a versatile linear light bullet with a vortex for any linear medium.

4.3 Experimental setup for collision between vortices in the temporal domain

Another goal in the thesis is to report the study of controlled collisions between two pulsed vortex beams in the time domain. In this experiment, an Airy-LG wave packet is generated to collide with a Gaussian-LG wave packet. The experimental setup is shown in Figure 4.6 which is very close to the setup in Figure 4.1. Similar pulse and beam shaping method are used to generate vortex wave packets. Ultrafast pulses from a mode-locked fiber laser are divided into three beam paths. One beam path (the bottom one) serves as the probe wave packet for the 3D measurement while the other beam (the middle path) will be converted into a Gaussian-LG wave packet by applying a spiral

plate. The third one (the top path) is shaped to a self-accelerating Airy pulse in the temporal time domain coupled with a vortex beam in the spatial domain produced by a SLM based pulse shaper and a beam shaping SLM in series. The resulting wave packet is a vortex Airy-LG wave packet. Two wave packets will be combined collinearly with a certain temporal delay between them. When they propagate in a strongly dispersive medium (the dispersive glass in Figure 4.6), the Airy-LG wave packet will accelerate to catch up and eventually overlap the Gaussian-LG wave packet in time. The location of the collision can be controlled by adjusting the delay line in the middle path. After propagating in a dispersive medium, temporally overlapped two wave packets serve as an object wave packet to be measured in 3D with the method presented in the previous chapter by overlapping the object wave packet with the probe wave packet.

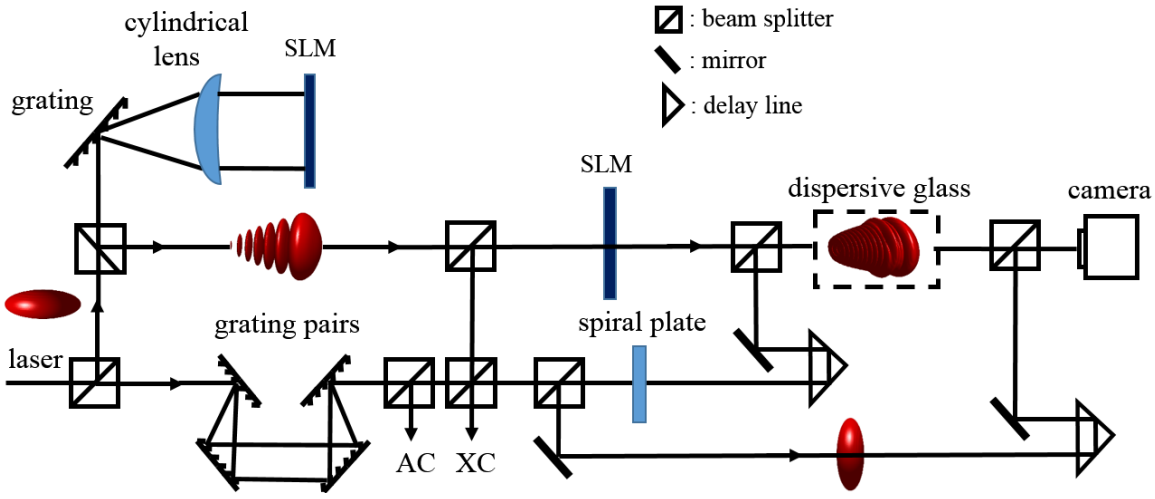

Figure 4.6 Experimental setup for collision between vortices in the temporal domain.

However, the experimental results were not entirely satisfactory. There are several problems that have to be carefully resolved in the future. First, it is very hard to align two wave packets perfectly collinear to obtain an ideal collision condition. If two beams are projected on a CCD camera with a small tilted angle (non-collinear), then a strong interference pattern appears. Second, two wave packets are required to be

overlapped not only in the spatial domain but also in the temporal domain. Therefore, in order to obtain ideal overlapping patterns, having a high-accurate and stable path-delay, such as a piezo actuator is essential. In the experiment, the delay path is neither accurate nor sufficiently stable. Due to such difficulties, the collided wave packet beam profiles are highly fringed. Moreover, beam patterns of the temporal collision are always highly fringed as shown Figure 4.7.

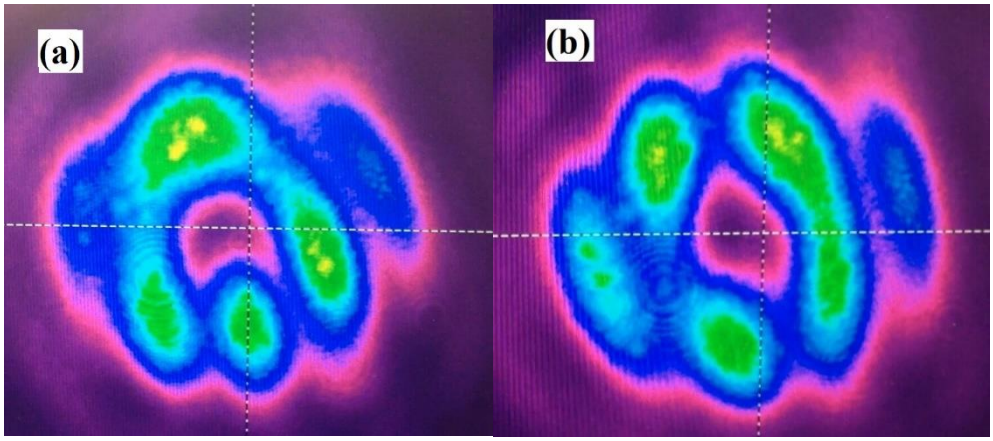

Figure 4.7 Two interference patterns ((a) and (b)) between two overlapping vortex beams on a CCD camera.

For the future work, more numerical simulations will be performed as discussed in Chapter II to help guide the experiments. Moreover, a more stable delay line will be considered for future experimental works.

CHAPTER V

CONCLUSIONS

This thesis is to demonstrate a versatile vortex linear light bullet as a 3D vortex Airy-Bessel wave packet. Its non-varying feature in linear propagation is verified by 3D measurement.

The experiment clearly demonstrates the vortex Airy-Bessel wave packet propagates without broadening in 3D in linear propagation. We believe that this wave packet can be adopted for many applications such as microscopies, nano-lithographies, nano-surgeries, etc.

The controlled collisions between pulsed optical vortices in the temporal domain is also studied in this thesis. Even though the time domain vortex collision is quite intriguing, the experiment is not yet satisfactory. Some suggestions are made in the thesis to improve the vortex collision experiments in the future.

BIBLIOGRAPHY

[1] B. E. A. Saleh and M. C. Teich, *Fundamentals of Photonics*. (John Wiley & Sons, 2007).

[2] A. Ashkin, J. M. Dziedzic, J. E. Bjorkholm and Steven Chu, "Observation of a single-beam gradient force optical trap for dielectric particles." *Opt. Lett.* **11**, 288 (1986).

[3] J. W. Goodman, *Introduction to Fourier Optics.* (McGraw-Hill; New York, 1996).

[4] J. Jia, C. Zhou, L. Liu, "Superresolution technology for reduction of the far-field diffraction spot size in the laser free-space communication system." *Opt. Commun*. **228**, 271 (2003).

[5] H. E. Hernández-Figueroa, M. Zamboni-Rached, and E. Recami, *Localized Waves.* (John Wiley & Sons, 2007).

[6] Y. Silberberg, "Collapse of optical pulses." *Opt. Lett.* **15**, 1282 (1990).

[7] X. Liu, L. J. Qian, and F. W. Wise, "Generation of Optical Spatiotemporal Solitons." *Phys. Rev. Lett.* **82**, 4631 (1999).

[8] L. F. Mollenauer, R. H. Stolen, and J. P. Gordon, "Experimental Observation of Picosecond Pulse Narrowing and Solitons in Optical Fibers." *Phys. Rev. Lett.* **45**, 1096 (1980).

[9] Y. S. Kivshar and G. P. Agrawal, *Optical Solitons*, (Elsevier's Science & Technology, 2003).

[10]M. Segev, B. Crosignani, A. Yariv, and B. Fischer, "Spatial Solitons in Photorefractive Media." *Phys. Rev. Lett*. **68**, 923 (1992).

[11] B. A. Malomed, D. Mihalache, F. W. Wise, and L. Torner, "Spatiotemporal optical solitons." *J. Opt. B* **7**, R53 (2005).

[12] J. Lu and J. F. Greenleaf, "Nondiffractiing X-waves. Exact solutions to free space scalar wave equation and their finite aperture realizations*." IEEE Trans. Ultrason. Ferroelec. Freq. Cont.* **39**, 19 (1992)

[13] M. A. Porras and P. Di Trapani, “Localized and stationary light wave modes in dispersive media,” *Phys. Rev. E* **69**, 066606 (2004).

[14] H. Sõnajalg, M. Rätsep, and P. Saari, “Demonstration of the Bessel-X pulse propagation with strong lateral and longitudinal localization in a dispersive medium.” *Opt. Lett*. **22**, 310 (1997).[15] M. A. Porras, “Diffraction-free and dispersion-free pulsed beam propagation in dispersive media.” *Opt. Lett.* **26**, 1364 (2001).

[16] G. A. Siviloglou, J. Broky, A. Dogariu, and D. N. Christodoulides, “Observation of accelerating Airy beams.” *Phys. Rev. Lett*. **99**, 213901 (2007).

[17] J. Broky, G. A. Siviloglou, A. Dogariu, and D. N. Christodoulides, “Self-healing properties of optical Airy beams.” *Opt. Express*. **16**, 12880 (2008).

[18] A. Chong, W. H. Renninger, D. N. Christodoulides, and F. W. Wise, “Airy-Bessel wave packets as versatile linear light bullets,” *Nature Photon.* **4**, 103 (2010).

[19] M. R. Dennis, K. O’Holleran, and M. J. Padgett, *Progress in Optics* (Elsevier B.V. 2009).

[20] K. Dholakia, G. Spalding and M. Macdonald, Optical tweezers: the next generation, *Physics World,* 31 (2002).

[21] Q. Zhan, “Properties of circularly polarized vortex beams,” *Opt. Lett.* **31**, 867 (2006).

[22] D. Mihalache, D. Mazilu, L. C. Crasovan, I. Towers, A. V. Buryak, B. A. Malomed, L. Torner, J. P. Torres, and F. Lederer, “Stable Spinning Optical Solitons in Three Dimensions.” *Phys. Rev. Lett*. **69**, 073902 (2002).

[23] D. Mihalache, D. Mazilu, L. C. Crasovan, I. Towers, A. V. Buryak, B. A. Malomed, L. Torner, J. P. Torres, and F. Lederer, “Stable three-dimensional spinning optical solitons supported by competing quadratic and cubic nonlinearities.” *Phys. Rev. E*. **66**, 016613 (2002).

[24] C. Rosales-Guzman, M. Mazilu, J. Baumgartl, V. Rodriguez-Fajardo, R. Ramos-Garcia and K. Dholakia*,* “Collision of propagating vortices embedded within Airy beams.” *J. Opt.* **15**, 044001 (2013).

[25] P. P. Banerjee and T. C. Poon, *Principles of Applied Optics*. (Aksen Associates, 1991).

[26] R. Paschotta, article on 'chromatic dispersion' in the *Encyclopedia of Laser Physics and Technology*, <https://www.rp-photonics.com/chromatic_dispersion.html>.

[27] G. P. Agrawal, *Nonlinear Fiber Optics*. (Academic Press, 1995).

[28] A. M. Weiner, *Ultrafast Optics*. (John Wiley & Sons, 2009).

[29] R. Trebino, *Frequency-Resolved Optical Grating: The Measurement of Ultrashort Laser Pulses*. (Springer Science & Business Media, 2000).

[30] Q. Cao, "Propagation Dynamics of Spatio-temporal Wave Packets." (Electronic Thesis, University of Dayton, 2014).

[31] D. McGloin and K. Dholakia, "Bessel beams: diffraction in a new light." *Contemporary Phys.*, 46, 15 (2005).

[32] J. Arlt, V. Garces-Chavez, W. Sibbett and K. Dholakia. "Optical micromanipulation using a Bessel light beam." *Opt. Commun*., **197**,239 (2001).
[33] J. Fan, E. Parra, I. Alexeev, K. Y. Kim, and H. M. Milchberg, "Tubular plasma generation with a high-power hollow Bessel beam." *Phys. Rev. E* **62**, R7603 (2000).

[34] J. Arlt and K. Dholakia, "Generation of high-order Bessel beam by use of an axicon", *Opt. Commun.*, **177**, 297 (2000).

[35] A. M. Weiner, "Ultrafast optical pulse shaping: A tutorial review." *Opt. Commun.,* **284**, 3669 (2011).

[36] D. P. Sprùnken, "A 2D Spatial Light Modulator for spatio-temporal shaping" Master Thesis for University of Twente.

[37] H. Li, I. V. Bazarov, B. M. Dunham, and F. W. Wise, "Three-dimensional laser pulse intensity diagnostic for photoinjectors," *Phys. Rev. ST Accel. Beams* **14**, 112802 (2011).

[38] Y. Li, S. Chemerisov, and J. Lewellen, "Laser pulse shaping for generating uniform three-dimensional ellipsoidal electron beams." *Phys. Rev. ST Accel. Beams* **12**, 020702 (2009).

[39] Q. Cao, C. Wan, and A. Chong, "Three-dimensional measurement of the Airy-Bessel wave packet propagation," in *Frontiers in Optics* 2014, (Optical Society of America, 2014), paper FTu5A.6.

[40] X. Huang, Q. Cao, H. Li, P. Li, C. Wan, and Andy Chong, "Generation of Versatile Vortex Linear Light Bullet," in *Frontiers in Optics* 2015, (Optical Society of America, 2015), paper JTu5A.11.